Computers and Structures 219 (2019) 1–15

Contents lists available at ScienceDirect

Computers and Structures

journal homepage: www.elsevier.com/locate/compstruc

Monolithic coupling of the implicit material point method with the finite element method

Eugenio Aulisa [a], Giacomo Capodaglio [b,*]

[a] Department of Mathematics & Statistics, Texas Tech University, USA
[b] Department of Scientific Computing, Florida State University, USA

ARTICLE INFO

Article history:
Received 31 January 2019
Accepted 19 April 2019
Available online 27 April 2019

Keywords:
Implicit material point method
Finite element method
Monolithic coupling
Automatic differentiation
MPM-FEM coupling

ABSTRACT

A monolithic coupling between the material point method (MPM) and the finite element method (FEM) is presented. The MPM formulation described is implicit, and the exchange of information between particles and background grid is minimized. The reduced information transfer from the particles to the grid improves the stability of the method. Once the residual is assembled, the system matrix is obtained by means of automatic differentiation. In such a way, no explicit computation is required and the implementation is considerably simplified. When MPM is coupled with FEM, the MPM background grid is attached to the FEM body and the coupling is monolithic. With this strategy, no MPM particle can penetrate a FEM element, and the need for computationally expensive contact search algorithms used by existing coupling procedures is eliminated. The coupled system can be assembled with a single assembly procedure carried out element by element in a FEM fashion. Numerical results are reported to display the performances and advantages of the methods here discussed.

1. Introduction

The material point method (MPM) is a numerical method for problems that involve large deformations and/or history dependent materials. It has been originally introduced in [1–3] by Sulsky et al. as an extension to solid mechanics of the hydrodynamics FLIP method [4]. The MPM has been applied to simulate numerous problems involving, for instance: membranes [5,6], granular materials [7,8], sea ice modeling [9], explosions [10], free surface flows [11], snow modeling [12], viscoelastic fluids [13], phase-change [14], fluid-structure interaction [15–17], and dynamic crack propagation [18]. The MPM exploits the advantages of both the Eulerian and the Lagrangian approaches. The body is discretized with a set of particles (or material points) and is positioned on a background grid, where the momentum equation is solved. The background grid may be chosen to be a finite element grid, because interpolating functions are used to transfer information from the particles to the grid and back. In the classical MPM, particles information is transferred to the background grid, where the momentum equation is solved. The new information obtained from the solution of the momentum equation at the grid nodes is used to update the values of displacement, velocity and acceleration at the particles. Then, the background grid is reset to its initial position. With such a method, the drawbacks of using a purely Lagrangian approach are avoided, because entanglement of the background grid is prevented by resetting it to its initial state after every time step. Moreover, the numerical dissipation associated with an Eulerian approach is eliminated, due to the absence of the convection term.

Historically, the MPM has been conceived as an explicit method. Compared to the extensive amount of explicit MPM formulations available in the literature, only a few efforts have been made so far to set the analysis in an implicit framework [14,19–26]. An implicit approach is desirable because it guarantees much larger time steps compared to what can be obtained with explicit methods, but more importantly the implicit formulation facilitates the monolithic coupling of the MPM with the FEM, which is the ultimate goal of the present work. As other existing implicit MPM formulations, here the assembly procedure for the problem on the background grid is carried out in a finite element fashion. The only difference between a standard FEM assembly is that, for elements of the background grid that enclose MPM particles, the quadrature points used for numerical integration are not the Gauss points as in standard FEM, but rather the particles themselves. The implicit MPM formulated here differs from existing implicit approaches [19,20,23,24], because the exchange of information between particles and grid is minimized by avoiding *unnecessary* projections

* Corresponding author. 400 Dirac Science Library, Department of Scientific Computing, Florida State University, Tallahassee, FL 32306, USA.
E-mail address: gcapodaglio@fsu.edu (G. Capodaglio).

https://doi.org/10.1016/j.compstruc.2019.04.006
0045-7949/

from the particles to the background grid nodes. In turn, as it is shown later, the inertial contribution is evaluated directly at the particles rather than at the grid nodes. This approach is consistent with an assembly procedure where the particles are used in place of the Gauss points. A drawback of using particles as quadrature points consists of instabilities that may arise due to inaccurate numerical integration, which may occur when an element of the background grid does not host enough particles. To overcome this issue, a *soft stiffness* matrix is added to the MPM system matrix as in [20]. In the present work, the magnitude of the soft stiffness contribution on a given element depends on how many particles the element itself and its neighbors are hosting. This is measured with appropriate flags whose determination procedure is discussed in Section 3.3. Once these flags are obtained, scaling factors associated with them are computed. The scaling factors are involved in the assembly procedure of the soft stiffness matrix and determine the weight of its contribution on a given element. Such a technique to compute the soft stiffness contributions represents a novel contribution of the present work and was not explored in [20]. Clearly, it is necessary to strike a balance between the need for numerical stability, given by larger soft stiffness contributions, and the desire for accuracy, which improves as the soft contributions tend to zero. To further improve numerical stability and simplify the implementation, the background grid is divided in active and inactive background grid. The former is composed of all the elements of the background grid that host at least one particle, whereas elements that do not host any particle are collected in the inactive background grid. The active background grid is what is actually used at a given instant of time to interpolate the particle instances from the grid. Contributions from nodes that belong exclusively to elements of the inactive background grid are assembled in a separate way using a lumped mass matrix. Details on this procedure are given in Section 3.3. Taking into account the inactive background grid contributions, we can avoid resizing the global system of equations every time a particle moves to a different element. Moreover, the solution corresponding to the lumped mass matrix block is inexpensive (one Jacobi iteration), because it corresponds to the inverse of a diagonal matrix. The introduction of the inactive background grid becomes especially useful for the monolithic MPM-FEM coupling, which is the ultimate goal of this paper, and its main novelty. Another feature of the proposed formulation resides on the use of implicit differentiation for the computation of the system matrix. After the residual is assembled, the system matrix is obtained differentiating the residual vector with the library Adept [27]. With such a tool, the system matrix does not have to be computed explicitly as in existing implicit MPM strategies, and the implementation is strongly simplified.

For the coupling of MPM and FEM, only very few studies are available in the literature [28–31]. For simplicity, it is assumed that the interaction to be simulated is that of two solid bodies: one undergoing large deformations, modeled with MPM and one subject to small deformations, modeled with FEM. Such a choice is justified by the respective advantages of the two discretization methods when applied to different deformation regimes. The assembly procedure is carried out according to a finite element strategy and automatic differentiation is used to obtain the coupled system matrix. The proposed monolithic algorithm solves simultaneously for the MPM and FEM unknowns in a unique solver, so that the two solid bodies are treated as a single continuum. To the best of our knowledge, the present work is the first to address a monolithic coupling between an MPM body and a FEM body. The stress balance and the kinematic conditions across the MPM-FEM interface are automatically satisfied, resulting in a coupling that is accurate, robust, and stable. To allow a simultaneous solution of MPM and FEM unknowns, a finite element grid attached to the FEM body is used as background grid for the MPM. With such a feature, the interface between the MPM body and the FEM body is automatically tracked. No MPM particle can penetrate a FEM element, and a great advantage in terms of computational time is obtained, because time consuming contact search algorithms are eliminated. All the algorithms proposed in this work are implemented in the in-house finite element library FEMuS [32].

The paper is structured as follows: in Section 2, the domain configurations later employed in the mathematical formulation are introduced. In Section 3, a detailed description of the implicit MPM formulation proposed is provided. The new features of our formulation and the complete numerical algorithm are presented and discussed. In Section 4, the monolithic coupling between MPM and FEM is addressed, and the characteristics of the coupled problem are laid out. In Section 5, an algorithm for the receding phase of the contact interaction is described. This algorithm is necessary in order to prevent *sticky* phenomena induced by our monolithic formulation for large values of the Young's modulus. The paper is concluded with Section 6, where numerical results are reported to illustrate the performances of the proposed algorithms.

2. Domain configurations

In this section, the domain configurations for the mathematical formulation are discussed. After a general description, the MPM domain and the FEM domain are identified. Then, the problem of the reset of the MPM background at the beginning of every time step is addressed, for both the uncoupled and the coupled case.

2.1. The three domain configurations

Three different domain configurations are used in the mathematical formulation. Schematics can be found in Fig. 1. The *undeformed configuration*, $\widehat{\Omega} \subset \mathbb{R}^d$, represents the position of the domain in its original state (at time $t = 0$). The *deformed configuration* $\Omega(t)$ refers to the domain in its deformed state for all $t \in [0, T]$. It is obtained from the undeformed configuration as follows: for all $\widehat{\boldsymbol{x}} \in \widehat{\Omega}$,

$$\boldsymbol{x}(\widehat{\boldsymbol{x}}, t) = \widehat{\boldsymbol{x}} + \boldsymbol{u}(\widehat{\boldsymbol{x}}, \boldsymbol{t}), \quad \text{for } \boldsymbol{t} \geqslant \boldsymbol{0}, \tag{1}$$

where $\boldsymbol{u}(\widehat{\boldsymbol{x}}, \boldsymbol{t})$ is the displacement field. The third configuration is the *reference configuration*, denoted by $\widetilde{\Omega}$. The reference configuration does not change in the time interval $(t^n, t^{n+1}]$, and it is obtained from the undeformed configuration: for all $\widehat{\boldsymbol{x}} \in \widehat{\Omega}$,

$$\widetilde{\boldsymbol{x}}(\widehat{\boldsymbol{x}}) = \widehat{\boldsymbol{x}} + \boldsymbol{u}^{reset}(\widehat{\boldsymbol{x}}), \quad \text{for } t \in (t^n, t^{n+1}]. \tag{2}$$

The field $\boldsymbol{u}^{reset}$ is the *reset displacement field* associated with the given time interval $(t^n, t^{n+1}]$. Any point in the deformed configuration can be obtained from the reference configuration: for all $\widetilde{\boldsymbol{x}} \in \widetilde{\Omega}$,

$$\boldsymbol{x}(\widetilde{\boldsymbol{x}}, t) = \widetilde{\boldsymbol{x}} + \widetilde{\boldsymbol{u}}(\widetilde{\boldsymbol{x}}, t), \quad \text{for } t \in (t^n, t^{n+1}], \tag{3}$$

where $\widetilde{\boldsymbol{u}}$ is the displacement field with respect to the reference configuration.

2.2. The MPM and the FEM domains

For all $t \in [0, T]$, let $\Omega_{mpm}(t)$ and $\Omega_b(t)$ be open and bounded subsets of $\mathbb{R}^d$. Assume that $\Omega_{mpm}(t) \subset \Omega_b(t)$ for all $t \in [0, T]$. From now on, $\Omega_{mpm}(t)$ represents the body discretized with the MPM particles. The set $\Omega_b(t)$ is discretized with a regular finite element grid $\mathcal{T}_b$ [33,34], used as a background grid for the MPM body. While $\Omega_{mpm}(t)$ may be subject to roto-translation and large deformations due to the movement of the MPM body, $\Omega_b(t)$ undergoes only lim-

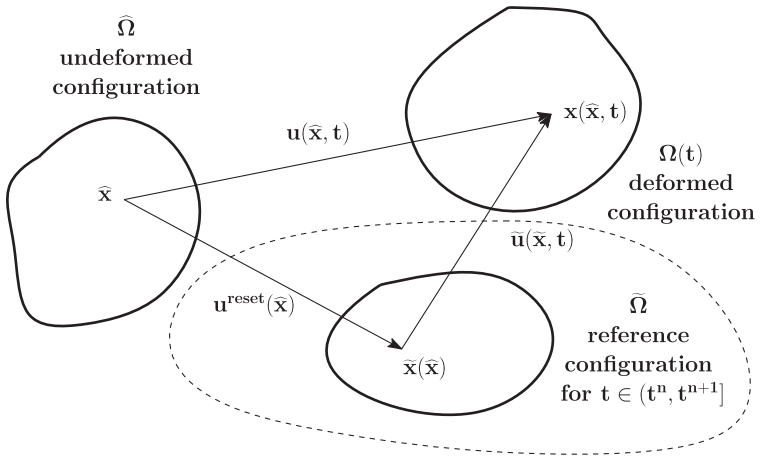

Fig. 1. Schematics for the domain configurations.

ited deformations, because it follows the MPM body motion only in the time interval $(t^n, t^{n+1}]$.

Denoting by $\mathcal{E}_p$ the element of the background grid that hosts a given particle p, we introduce

$$\Omega_{ab}(t) := \bigcup_{\mathcal{E}\in\mathcal{T}_{ab}} \mathcal{E} = \bigcup_{p=1}^{N_p} \mathcal{E}_p, \tag{4}$$

where $t \in (t^n, t^{n+1}]$, and $\mathcal{T}_{ab} \subset \mathcal{T}_b$ is the active background grid, composed of all elements $\mathcal{E}$ of $\mathcal{T}_b$ that host at least one particle p. Similarly, we define $\mathcal{T}_{ib} := \mathcal{T}_b \setminus \mathcal{T}_{ab}$ to be the inactive background grid, composed of all elements of $\mathcal{T}_b$ that do not enclose any particle. Schematics of the grids here described are shown in Fig. 2, where the grid $\mathcal{T}_{fem}$ used to discretize the FEM body has the darkest color, the inactive background grid $\mathcal{T}_{ib}$ has the intermediate color and the active background grid $\mathcal{T}_{ab}$ has the lightest color.

By definition, $\Omega_{mpm}(t) \subseteq \Omega_{ab}(t) \subseteq \Omega_b(t)$. We call $\Omega_{ab}(t)$ the *MPM domain*, because the MPM momentum equation is solved only on the active background grid $\mathcal{T}_{ab}$.

The open and bounded set $\Omega_{fem}(t) \subset \mathbb{R}^d$ is used to characterize both the body discretized with FEM and the FEM domain. The interfaces between the FEM domain and the background grid $\Omega_b(t)$ and between the FEM domain and the active background grid $\Omega_{ab}(t)$ that arise during the coupling procedure are indicated with the letters Γ and Γ_a, respectively.

2.3. Definition of the reset displacement field

In the classical MPM method, where no coupling between MPM and FEM occurs, at the beginning of each time step interval $(t^n, t^{n+1}]$, the set $\Omega_b(t)$ is reset to its undeformed configuration, $\widehat{\Omega}_b$, to avoid mesh entanglement. Namely, for any $t \in (t^n, t^{n+1}]$, if I refers to any node of the grid, the grid displacement $\boldsymbol{u}_I$ associated to the node I is such that

$$\lim_{t\to(t^n)^+} \boldsymbol{u}_I(t) = \mathbf{0}. \tag{5}$$

Moreover, in general

$$\lim_{t\to(t^n)^-} \boldsymbol{u}_I(t) = \boldsymbol{u}_I(t^n) \neq \mathbf{0}, \tag{6}$$

and as a result $\boldsymbol{u}_I(t)$ is discontinuous in time. On the other hand, in the classical uncoupled FEM method, the grid follows the solid body deformation and its displacement is continuous in time

$$\lim_{t\to(t^n)^-} \boldsymbol{u}_I(t) = \boldsymbol{u}_I(t^n) = \lim_{t\to(t^n)^+} \boldsymbol{u}_I(t). \tag{7}$$

With a monolithic coupling approach, there is a unique displacement field defined on the MPM background grid and on the finite element grid discretizing the FEM body. Hence, when the coupling between MPM and FEM is considered, the displacement at the grid points of $\mathcal{T}_b$ that lie on the interface Γ between $\Omega_b(t)$ and the FEM body cannot be reset to zero.

When MPM is coupled with FEM, the background grid has to fulfill the following constraints: in the FEM domain and on the interface Γ, it has to follow the solid deformation; in the MPM domain, in order to enforce domain continuity, it has to follow the deformation of Γ, coming from the FEM domain. Moreover, to avoid mesh entanglement, it is desirable to reset the background grid to a configuration similar to the undeformed configuration on all MPM nodes that are sufficiently far from Γ.

The background grid constraints are satisfied with the following definition of the reset displacement field $\boldsymbol{u}_I^{reset}$. Let $\mathcal{I}$ be the set of grid points of $\mathcal{T} = \mathcal{T}_b \cup \mathcal{T}_{fem}$, where $\mathcal{T}_{fem}$ denotes the finite element grid used to discretize the FEM body. For all $t \in (t^n, t^{n+1}]$, the reset displacement field satisfies

$$\begin{cases} \boldsymbol{u}_I^{reset} = \lim\limits_{t\to(t^n)^-} \boldsymbol{u}_I(t), & \text{if } \boldsymbol{x}_I \in \Omega_{\boldsymbol{fem}}(\boldsymbol{t}) \\ \nabla\cdot\left(\nabla \boldsymbol{u}_I^{\boldsymbol{reset}} + \left(\nabla \boldsymbol{u}_I^{\boldsymbol{reset}}\right)^{\boldsymbol{T}}\right) = \mathbf{0}, & \text{if } \boldsymbol{x}_I \in \Omega_{\boldsymbol{b}}(\boldsymbol{t}) \setminus \Gamma \end{cases} \tag{8}$$

where $\boldsymbol{x}_I$ denotes the position of node $I \in \mathcal{I}$. When MPM is coupled with FEM, Eq. (5) is replaced with

$$\lim_{t\to(t^n)^+} \boldsymbol{u}_I(t) = \boldsymbol{u}_I^{reset}. \tag{9}$$

In this way, the continuity of the domain is preserved across Γ, and the grid $\mathcal{T}_b$ follows the solid body deformation on $\Omega_{fem}(t)$, resulting in a continuous displacement field $\boldsymbol{u}_I(t)$. As a consequence of Eq. (9), at the beginning of each time step, the deformed configuration of the background grid coincides with its reference configuration, although it is in general different from its undeformed configuration $\widehat{\Omega}_b$. To fulfill the classical MPM requirement in Eq. (5), a new MPM displacement field based on the reference background grid configuration is defined as

$$\widetilde{\boldsymbol{u}}_I(t) = \boldsymbol{u}_I(t) - \boldsymbol{u}_I^{reset}. \tag{10}$$

By Eq. (9), this new field satisfies

$$\lim_{t\to(t^n)^+} \widetilde{\boldsymbol{u}}_I(t) = \mathbf{0},$$

as in the classical uncoupled MPM method.

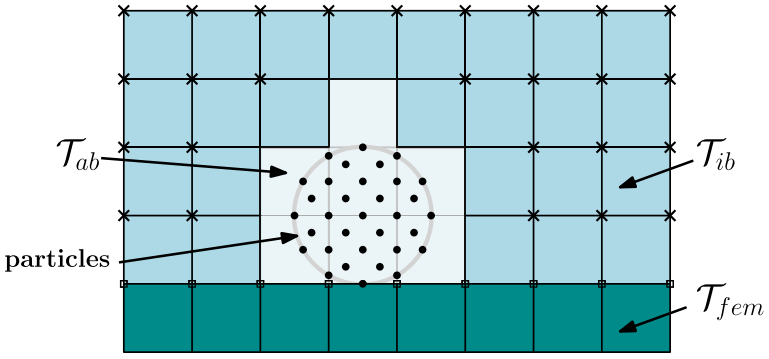

Fig. 2. Schematics of triangulations and domains used in the MPM-FEM coupled problem. The nodes marked with a cross belong exclusively to the inactive background grid $\mathcal{T}_{ib}$, whereas those marked with a box are the nodes at the interface between the MPM background grid $\mathcal{T}_b$ and the FEM grid $\mathcal{T}_{fem}$.

3. Implicit material point algorithm

The mathematical formulation of the proposed implicit material point and the complete numerical algorithm are described in this section.

3.1. Mathematical formulation

For ease of notation, during the rest of this paper, the time dependence of Ω_{mpm}, Ω_{ab}, and of the fields involved in the formulation is not made explicit. The mass conservation is automatically satisfied by the material point method [35], therefore the governing equations for the MPM body consist of momentum conservation with appropriate boundary and initial conditions. For simplicity, we consider zero boundary conditions for displacement and normal stress

$$\begin{aligned} &\rho\,\ddot{\boldsymbol{u}} - \nabla\cdot\boldsymbol{\sigma} = \rho\,\boldsymbol{b}, && \text{in } \Omega_{mpm}\times[0,T],\\ &\boldsymbol{\sigma}\cdot\boldsymbol{n} = 0, && \text{on } \partial\Omega_{mpm,trac}\times[0,T],\\ &\boldsymbol{u} = 0, && \text{on } \partial\Omega_{mpm,disp}\times[0,T],\\ &\boldsymbol{u}(\boldsymbol{x},0) = \boldsymbol{u}_0, \quad \dot{\boldsymbol{u}}(\boldsymbol{x},0) = \dot{\boldsymbol{u}}_0 && \text{in } \Omega_{mpm}. \end{aligned} \tag{11}$$

In Eq. (11), $\boldsymbol{u}$ represents the displacement, $\boldsymbol{\sigma}$ is the Cauchy stress tensor, ρ is the MPM body density, $\boldsymbol{b}$ is the body force per unit mass, $\dot{\boldsymbol{u}}$ is the velocity, $\ddot{\boldsymbol{u}}$ is the acceleration and $\boldsymbol{n}$ is the unit outward normal of the boundary $\partial\Omega_{mpm,trac}$, that represents the traction boundary. Similarly, $\partial\Omega_{mpm,disp}$ represents the portion of the boundary where displacement boundary conditions are prescribed. Constitutive equations for the Cauchy stress need to be added to complete the above set of equations. We describe the MPM solid bodies as Neo-Hookean materials, with the Cauchy stress tensor given by [36]

$$\boldsymbol{\sigma} = \lambda\frac{\log(J)}{J}\boldsymbol{I} + \frac{\mu}{J}(\boldsymbol{B}-\boldsymbol{I}). \tag{12}$$

In Eq. (12), λ is Lamé's first parameter, $\boldsymbol{I}$ is the identity matrix, μ is the shear modulus, $\boldsymbol{B} = \boldsymbol{F}\boldsymbol{F}^T$ is the left Cauchy-Green strain tensor, $\boldsymbol{F}$ is the deformation gradient and $J = \det(\boldsymbol{F})$. Let $\Delta U = \left\{\boldsymbol{\delta u} \in \boldsymbol{H}^1(\Omega_{mpm}) \mid \boldsymbol{\delta u}|_{\partial\Omega_{mpm,disp}} = 0\right\}$. The virtual displacements are chosen as test functions for the weak formulation, which reads

$$\int_{\Omega_{mpm}} \rho\left(\ddot{u}_i\,\delta u_i + \sum_{j=1}^{d}\sigma^s_{ij}\frac{\partial\delta u_i}{\partial x_j} - b_i\,\delta u_i\right)dV = 0, \text{ for } i = 1,\dots,d. \tag{13}$$

where $\sigma^s_{ij} = \sigma_{ij}/\rho(\boldsymbol{x},t)$ is the specific Cauchy stress. The interested reader can consult [35] for more details on how to derive the above weak formulation. The integrals involved in Eq. (13) can be transformed in sums if the MPM density ρ is approximated using the Dirac delta function δ as

$$\rho(\boldsymbol{x},t) \approx \sum_{p=1}^{N_p} m_p\,\delta(\boldsymbol{x}-\boldsymbol{x}_p(t)), \tag{14}$$

where $\boldsymbol{x}_p$ denotes the position of particle p, and N_p represents the total number of particles used to discretize Ω_{mpm}. Substituting Eq. (14) in Eq. (13) we obtain

$$\sum_{p=1}^{N_p} m_p\left[\ddot{u}_i(\boldsymbol{x}_p)\delta u_i(\boldsymbol{x}_p) + \sum_{j=1}^{d}\sigma^s_{ij}(\boldsymbol{x}_p)\frac{\partial\delta u_i}{\partial x_j}(\boldsymbol{x}_p) - b_i(\boldsymbol{x}_p)\delta u_i(\boldsymbol{x}_p)\right] = 0. \tag{15}$$

In the above equation, $\sigma^s_{ij}(\boldsymbol{x}_p) = J(\boldsymbol{x}_p)\,\sigma_{ij}(\boldsymbol{x}_p)/\rho_0$, where ρ_0 is the density of the MPM body in the initial, undeformed configuration.

Remark 1. Because the MPM body is discretized with particles, the values of the fields at the particles can be identified with the particle fields. For instance, $\ddot{u}_i(\boldsymbol{x}_p) = \ddot{u}_{i,p}$, where $\ddot{u}_{i,p}$ represents the i-th component of the acceleration of particle p.

Considering the above remark, Eq. (15) can be rewritten as

$$\sum_{p=1}^{N_p} m_p\left[\ddot{u}_{i,p}\delta u_i(\boldsymbol{x}_p) + \sum_{j=1}^{d}\sigma^s_{ij,p}\frac{\partial\delta u_i}{\partial x_j}(\boldsymbol{x}_p) - b_{i,p}\delta u_i(\boldsymbol{x}_p)\right] = 0. \tag{16}$$

The weak formulation for the MPM equations in Eq. (16) is solved numerically employing the active background grid $\mathcal{T}_{ab}$. For any given particle p, an interpolation from the nodes of the element $\mathcal{E}_p \in \mathcal{T}_{ab}$ that encloses p is performed. This step is part of the assembly procedure of the background grid system and is discussed within the complete numerical algorithm.

3.2. Implicit time integration

The Newmark-beta integrator is adopted for the numerical integration of $\ddot{u}_{i,p}$ in Eq. (16). If $\boldsymbol{u}_p^{n+1}$ denotes the particle displacement at time t^{n+1} and the same notation is also adopted for particle velocity and acceleration, the method gives

$$\dot{\boldsymbol{u}}_p^{n+1} = \dot{\boldsymbol{u}}_p^n + (1-\gamma)\,\Delta t\,\ddot{\boldsymbol{u}}_p^n + \gamma\,\Delta t\,\ddot{\boldsymbol{u}}_p^{n+1}, \tag{17}$$

$$\boldsymbol{u}_p^{n+1} = \boldsymbol{u}_p^n + \Delta t\,\dot{\boldsymbol{u}}_p^n + \frac{1}{2}\Delta t^2(1-2\beta)\ddot{\boldsymbol{u}}_p^n + \Delta t^2\beta\ddot{\boldsymbol{u}}_p^{n+1}, \tag{18}$$

for $\gamma\in[0,1]$, $\beta\in[0,0.5]$ and $\Delta t = t^{n+1}-t^n$. It follows that,

$$\ddot{\boldsymbol{u}}_p^{n+1} = \frac{1}{\beta\Delta t^2}\left(\boldsymbol{u}_p^{n+1}-\boldsymbol{u}_p^n\right) - \frac{1}{\beta\Delta t}\dot{\boldsymbol{u}}_p^n - \frac{1-2\beta}{2\beta}\ddot{\boldsymbol{u}}_p^n. \tag{19}$$

3.3. The numerical algorithm

The complete numerical algorithm for the implicit MPM scheme presented in this paper is described next. The algorithm is divided into a series of stages and it is set in a parallel framework where different processes handle their own share of the background grid and particles. For ease of reading, a flow chart is shown in Fig. 3.

- **Initialization of the MPM particles**.
  The first step consists of particle initialization. We assume that the total number of particles N_p, the volume V_p associated with each particle, and the initial density ρ_0 of the undeformed MPM body are given. With this information, the mass of each particle is computed as $m_p = \rho_0 V_p$. The initial position $\boldsymbol{x}_p$ of each particle p is also known. The values of displacement $\boldsymbol{u}_p$ and velocity $\dot{\boldsymbol{u}}_p$ of the particles are initialized as in Eq. (11). The acceleration $\ddot{\boldsymbol{u}}_p$ is set to zero, whereas the deformation gradient $\boldsymbol{F}_p$ at the particle is initialized to a given initial value $\boldsymbol{F}_p^0 := \boldsymbol{F}_p(0)$. Once a particle has been placed on the FEM background grid, the element $\mathcal{E}_p$ on the background grid that hosts the particle is determined, using the point locating method described in [37].
- **Assembly and solution of the background grid system**.
  For this step, it is assumed that the particle instances at time t^n are known and that those at time t^{n+1} have to be determined. Let $\mathcal{I}_b = \{1, \dots, N_b\}$ be the set of grid points of $\mathcal{T}_b$. Let $\mathcal{I}_{ab}$ be the set of grid points of $\mathcal{T}_{ab}$ and $\mathcal{I}_{ib} := \mathcal{I}_b \setminus \mathcal{I}_{ab}$. The assembly procedure is carried out differently depending on whether a node of the background grid belongs to the active or inactive background grid. Both assembly procedures are described in detail in the next steps.
  1. **Assembly of the active background grid contributions**.
     A loop on the particles is executed to assemble the MPM contributions. Given a particle p from the loop, the element $\mathcal{E}_p$ on the active background grid $\mathcal{T}_{ab}$ that is currently hosting the particle is extracted. In a sense, this procedure is similar to a standard FEM procedure because the assembly is still performed in an element-by-element fashion. The differences are that now particles are used as quadrature points instead of Gauss points, and that the quadrature contributions on a given element are not computed sequentially, because particles that belong to the same element may not be all grouped together in the particle loop.

Remark 2. Unlike other existing implicit MPM formulations [19,20,23,24], our assembly procedure does not start with a mapping from the particles to the grid nodes. The Newmark scheme in Eq. (19) is used directly on the particle instances instead of the grid instances as existing strategies do. For this reason, no mapping from the particles to the background grid is necessary.

According to a FEM approach, the particle virtual displacement in Eq. (16) can be obtained through interpolation from the nodes of $\mathcal{E}_p$. If $N_{\mathcal{E}_p}$ denotes the number of nodes of element $\mathcal{E}_p$, we have $\delta u_{i,p} = \sum_{I_{\mathcal{E}_p}=1}^{N_{\mathcal{E}_p}} \delta u_{i,I_{\mathcal{E}_p}} \phi_{I_{\mathcal{E}_p}}(\boldsymbol{x}_p)$, where $\delta u_{i,I_{\mathcal{E}_p}}$ represents the nodal value of the virtual displacement at node $I_{\mathcal{E}_p}$ and $\phi_{I_{\mathcal{E}_p}}$ is the finite element test function associated with node $I_{\mathcal{E}_p}$. Thanks to the arbitrariness of $\delta u_{i,I_{\mathcal{E}_p}}$ and the fact that by definition $\delta u_{i,I_{\mathcal{E}_p}} = 0$ on $\mathcal{E}_p \cap \partial\Omega_{mpm,disp}$, the equation for the $I_{\mathcal{E}_p}$-th entry of the local residual vector associated with MPM contributions is obtained from Eq. (16)

$$r_{mpm,i,I_{\mathcal{E}_p}} := \sum_{p=1}^{N_p} m_p \left[\ddot{u}_{i,p} \phi_{I_{\mathcal{E}_p}}(\boldsymbol{x}_p) + \left(\sum_{j=1}^{d} \sigma^s_{ij,p} \frac{\partial \phi_{I_{\mathcal{E}_p}}}{\partial x_j}(\boldsymbol{x}_p) \right) - b_{i,p} \phi_{I_{\mathcal{E}_p}}(\boldsymbol{x}_p) \right] = 0, \quad I_{\mathcal{E}_p} = 1, \dots N_{\mathcal{E}_p}. \tag{20}$$

In general, it may not be necessary to interpolate from the grid nodes to the particles to evaluate the body force at the particles. For instance, if the body force is a gravitational force, then no interpolation is necessary and its value at the particles can be computed directly. Therefore, the values of the body force remain evaluated at the particles, and interpolation may be performed if needed. The term $\ddot{u}_{i,p}$ in Eq. (16) is computed with the Newmark scheme in Eq. (19). Specifically, $\ddot{u}_{i,p}$ is given by

$$\ddot{u}_{i,p} = \frac{1}{\beta \Delta t^2} \widetilde{u}_{i,g}(\boldsymbol{x}_p) - \frac{1}{\beta \Delta t} \dot{u}^n_{i,p} - \frac{1-2\beta}{2\beta} \ddot{u}^n_{i,p}, \tag{21}$$

where $\widetilde{u}_{i,g}(\boldsymbol{x}_p)$ denotes the reference background grid displacement value at $\boldsymbol{x}_p$, defined as

$$\widetilde{u}_{i,g}(\boldsymbol{x}_p) := \sum_{I_{\mathcal{E}_p}=1}^{N_{\mathcal{E}_p}} \widetilde{u}_{i,I_{\mathcal{E}_p}} \widetilde{\phi}_{I_{\mathcal{E}_p}}(\boldsymbol{x}_p), \tag{22}$$

where $\widetilde{u}_{i,I_{\mathcal{E}_p}}$ is as in Eq. (10). The value of $\sigma^s_{ij,p}$ in Eq. (20) refers to the specific Cauchy stress obtained with a partial interpolation from the grid nodes, as in [19]. Recalling the constitutive law in Eq. (12), $\sigma^s_{ij,p}$ is given by

$$\boldsymbol{\sigma}^s_p = \frac{\lambda \log(J_p)}{\rho J_p} \boldsymbol{I} + \frac{\mu}{J_p} (\boldsymbol{B}_p - \boldsymbol{I}), \tag{23}$$

where $J_p = \det(\boldsymbol{F}_p), \boldsymbol{B}_p = \boldsymbol{F}_p (\boldsymbol{F}_p)^T$ and

$$\boldsymbol{F}_p = \left(\widetilde{\nabla} \widetilde{\boldsymbol{u}}_g(\boldsymbol{x}_p) + \boldsymbol{I} \right) \boldsymbol{F}^n_p. \tag{24}$$

In Eq. (24), $\widetilde{\nabla}$ represents the Del operator with respect to the reference configuration and $\widetilde{\nabla} \widetilde{\boldsymbol{u}}_g(\boldsymbol{x}_p)$ is the background grid displacement gradient with respect to the reference configuration, evaluated at $\boldsymbol{x}_p$, defined as

$$\widetilde{\nabla} \widetilde{u}_{ij,g}(\boldsymbol{x}_p) := \sum_{I_{\mathcal{E}_p}=1}^{N_{\mathcal{E}_p}} \widetilde{u}_{i,I_{\mathcal{E}_p}} \frac{\partial \widetilde{\phi}_{I_{\mathcal{E}_p}}}{\partial \widetilde{x}_j}(\boldsymbol{x}_p). \tag{25}$$

The next step consists of determining the scaling factors for the assembly of the *soft stiffness* matrix. Such factors depend on flags $M_{\mathcal{E}}$ assigned to each element of the active background grid $\mathcal{T}_{ab}$. The value of a flag depends on the element's relative position with respect to the MPM particles. Let $N_{\mathcal{E}}$ be the total number of degrees of freedom associated with an element $\mathcal{E}$ on the active background grid. The value of $M_{\mathcal{E}}$ is initialized to $N_{\mathcal{E}}$ and is modified according to the following rule: for any node $I_{\mathcal{E}}$ of $\mathcal{E}$ that also belongs to an element of $\mathcal{T}_{ib}$, $M_{\mathcal{E}}$ is decreased by one.
Next, a loop on all elements that are part of the active background grid is carried out in the standard finite element fashion, to compute the soft stiffness contribution of the local residual

$$r_{soft,i,I_{\mathcal{E}}} := \mu C_{\mathcal{E}} \int_{\mathcal{E}} \left[\widetilde{\nabla} \widetilde{\boldsymbol{u}} + \left(\widetilde{\nabla} \widetilde{\boldsymbol{u}} \right)^T \right]_i \cdot \widetilde{\nabla} \widetilde{\phi}_{I_{\mathcal{E}}} dV, \text{ for } \quad I_{\mathcal{E}} = 1, \dots, N_{\mathcal{E}}. \tag{26}$$

The value of $C_{\mathcal{E}}$ is a measure of the magnitude of the soft stiffness contribution and it depends on the flags $M_{\mathcal{E}}$ previously determined. As a general rule, $C_{\mathcal{E}}$ is a non-increasing function of $M_{\mathcal{E}}$, and it is zero for any element fully surrounded by elements containing particles. The soft stiffness improves stability while decreasing accuracy, and it is recommended to keep $C_{\mathcal{E}}$ as small as possible.

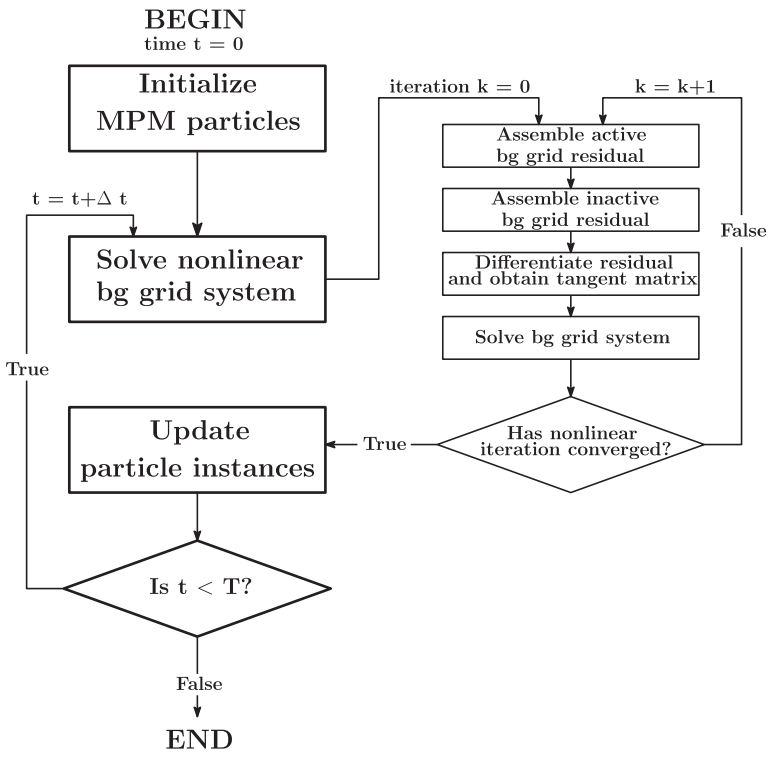

Fig. 3. Flow chart of the numerical algorithm in Section 3.3. The shorthand bg stands for background.

Examples of values for $C_{\mathcal{E}}$ are given in Section 6.

For all nodes that belong to $\mathcal{I}_{ib}$ (so exclusively to the inactive background grid), a fictitious equation is assembled using a lumped mass matrix, as it is shown next.

2. **Assembly of the inactive background grid contributions**. Let $\mathcal{E}$ be any element in $\mathcal{T}_{ib}$. Then, for any node $I_{\mathcal{E}} \in \mathcal{I}_{ib}$, the local residual is computed as the product of a lumped mass matrix with the nodal displacement vector, as follows

$$r_{mass,i,I_{\mathcal{E}}} := \int_{\mathcal{E}} u_{i,I_{\mathcal{E}}} \widehat{\phi}_{I_{\mathcal{E}}} dV, \tag{27}$$

for $I_{\mathcal{E}} = 1, \ldots, N_{\mathcal{E}}, I_{\mathcal{E}} \in \mathcal{T}_{ib}$. Recall that $\mathcal{I}_{ib}$ contains only the nodes that belong exclusively to the inactive background grid, so nodes that are shared with elements that include at least one particle are excluded from the inactive background grid contribution.

3. **Differentiation of the residual vector**.

Let $\boldsymbol{r}_{mpm,\mathcal{E}_p} = \left[r_{mpm,1,1}, r_{mpm,1,2}, \ldots, r_{mpm,d,N_{\mathcal{E}_p}}\right]$ denote the local residual vector associated with the MPM contributions from element $\mathcal{E}_p$. The global MPM residual vector is denoted by

$$\boldsymbol{r}_{mpm} = \left[r_{mpm,1,1}, r_{mpm,1,2}, \ldots, r_{mpm,d,N_g}\right]$$

and is obtained in the standard finite element fashion, adding the entries of the local MPM residual vectors associated with the same global nodes. The global soft residual vector $\boldsymbol{r}_{soft}$ and the global mass residual vector $\boldsymbol{r}_{mass}$ are constructed in the same way. It is important from an implementational point of view to ensure that the three global residual have matching dimensions and that they are all initialized to zero. Next, the global residual vector $\boldsymbol{r}$ for the background grid system is defined as

$$\boldsymbol{r} = \boldsymbol{r}_{mass} + \boldsymbol{r}_{soft} + \boldsymbol{r}_{mpm}. \tag{28}$$

Let $\boldsymbol{u}^{k+1} = \left[u_{1,1}^{k+1}, u_{1,2}^{k+1}, \ldots, u_{d,N_g}^{k+1}\right]$ represent the vector of displacement values at the grid nodes at iteration $k+1$, then $\boldsymbol{r} = \boldsymbol{r}(\boldsymbol{u}^{k+1})$ is a nonlinear function of $\boldsymbol{u}^{k+1}$ and the values of the displacement at the grid nodes are given by the solution of the nonlinear equation

$$\boldsymbol{r}(\boldsymbol{u}^{k+1}) = 0. \tag{29}$$

Writing $\boldsymbol{u}^{k+1} = \boldsymbol{u}^k + \Delta\boldsymbol{u}^{k+1}$ and expanding Eq. (29) in a Taylor series around $\boldsymbol{u}^k$, the following equation is obtained

$$0 = \boldsymbol{r}(\boldsymbol{u}^{k+1}) = \boldsymbol{r}(\boldsymbol{u}^k) + \frac{\partial \boldsymbol{r}(\boldsymbol{u}^k)}{\partial \boldsymbol{u}} \Delta\boldsymbol{u}^{k+1} + O\left(\left(\Delta\boldsymbol{u}^{k+1}\right)^2\right). \tag{30}$$

Neglecting the higher order terms, a linear system of equations is recovered

$$\boldsymbol{K}(\boldsymbol{u}^k)\Delta\boldsymbol{u}^{k+1} = -\boldsymbol{r}(\boldsymbol{u}^k), \tag{31}$$

where $\boldsymbol{K}(\boldsymbol{u}^k) := \frac{\partial \boldsymbol{r}(\boldsymbol{u}^k)}{\partial \boldsymbol{u}}$ is the background grid stiffness matrix, $\Delta\boldsymbol{u}^{k+1}$ is the solution increment vector and the forcing term $-\boldsymbol{r}(\boldsymbol{u}^k)$ is the negative residual vector associated with the solution at the previous iteration. In the numerical implementation, the tangent stiffness matrix $\boldsymbol{K}(\boldsymbol{u}^k)$ is obtained using automatic differentiation, a tool provided by the Adept library [27], and its computation is exact up to machine precision. Once the residual has been assembled, no explicit calculation has to be carried out to obtain such a matrix.

After an appropriate reordering of the grid nodes, Eq. (31) can be written as the following block system

$$\begin{bmatrix} \boldsymbol{K}_{ab}(\boldsymbol{u}_{ab}^k) & \boldsymbol{0} \\ \boldsymbol{0} & \boldsymbol{M}_{ib} \end{bmatrix} \begin{bmatrix} \Delta\boldsymbol{u}_{ab}^{k+1} \\ \Delta\boldsymbol{u}_{ib}^{k+1} \end{bmatrix} = \begin{bmatrix} -\boldsymbol{r}_{ab}(\boldsymbol{u}_{ab}^k) \\ -\boldsymbol{r}_{ib}(\boldsymbol{u}_{ib}^k) \end{bmatrix}, \tag{32}$$

where

$$\begin{aligned}
&\boldsymbol{K}_{ab}\left(\boldsymbol{u}_{ab}^{k}\right) := \boldsymbol{K}_{soft}\left(\boldsymbol{u}_{ab}^{k}\right) + \boldsymbol{K}_{mpm}\left(\boldsymbol{u}_{ab}^{k}\right),\\
&\boldsymbol{r}_{ab}\left(\boldsymbol{u}_{ab}^{k}\right) := \boldsymbol{r}_{soft}\left(\boldsymbol{u}_{ab}^{k}\right) + \boldsymbol{r}_{mpm}\left(\boldsymbol{u}_{ab}^{k}\right),\\
&\boldsymbol{K}_{soft}\left(\boldsymbol{u}_{ab}^{k}\right) := \frac{\partial \boldsymbol{r}_{soft}\left(\boldsymbol{u}_{ab}^{k}\right)}{\partial \boldsymbol{u}_{ab}}, \quad \boldsymbol{K}_{mpm}\left(\boldsymbol{u}_{ab}^{k}\right) := \frac{\partial \boldsymbol{r}_{mpm}\left(\boldsymbol{u}_{ab}^{k}\right)}{\partial \boldsymbol{u}_{ab}},\\
&\boldsymbol{r}_{ib}\left(\boldsymbol{u}_{ib}^{k}\right) := \boldsymbol{r}_{mass}\left(\boldsymbol{u}_{ib}^{k}\right), \quad \boldsymbol{M}_{ib} := \frac{\partial \boldsymbol{r}_{mass}\left(\boldsymbol{u}_{ib}^{k}\right)}{\partial \boldsymbol{u}_{ib}}.
\end{aligned} \tag{33}$$

4. **Solution of the background grid system**.
   Let $\Delta \boldsymbol{u}^{k+1}$ denote the solution of system (32). The displacement at the grid is advanced as $\boldsymbol{u}^{k+1} = \boldsymbol{u}^{k} + \Delta \boldsymbol{u}^{k+1}$. If the displacement falls below a prescribed tolerance, the algorithm moves to the next stage, otherwise further iterations are carried out.

- **Update of Particle Instances**.
  As for the assembly procedure, this step begins with a loop on the particles. Then, for a given particle p, the element $\mathcal{E}_p$ that hosts it is extracted. The deformation gradient is updated in the following way

$$\boldsymbol{F}_{p}^{n+1} = \left(\widetilde{\nabla}\,\widetilde{\boldsymbol{u}}_{g}^{n+1}\left(\boldsymbol{x}_{p}\right) + \boldsymbol{I}\right)\boldsymbol{F}_{p}^{n}, \tag{34}$$

where

$$\widetilde{\boldsymbol{u}}_{g}^{n+1}\left(\boldsymbol{x}_{p}\right) := \sum_{I_{\mathcal{E}_p}=1}^{N_{\mathcal{E}_p}} \widetilde{\boldsymbol{u}}_{I_{\mathcal{E}_p}}^{n+1}\,\widetilde{\phi}_{I_{\mathcal{E}_p}}\left(\boldsymbol{x}_{p}\right). \tag{35}$$

The particle displacement is obtained via interpolation from the displacement $\widetilde{\boldsymbol{u}}_{I}$ at the nodes of $\mathcal{E}_p$. Namely, $\boldsymbol{u}_{p}^{n+1} \equiv \widetilde{\boldsymbol{u}}_{g}^{n+1}\left(\boldsymbol{x}_{p}\right)$. With this information and the particle instances at the previous instant of time, velocity and acceleration are updated using the Newmark scheme in Eqs. (17) and (19) respectively. Finally, the particle positions are updated as $\boldsymbol{x}_{p}^{n+1} = \boldsymbol{x}_{p}^{n} + \boldsymbol{u}_{p}^{n+1}$.

4. Monolithic coupling between MPM and FEM

In this section, the solid-solid monolithic coupling between the proposed implicit material point method and the finite element method is described. The two solid bodies are treated as a single continuum, and a shared finite element grid is used for the FEM body and the MPM background grid. In this way, the MPM background grid follows the solid deformations and the interface between MPM and FEM bodies is automatically tracked. This monolithic approach eliminates the need for time consuming contact algorithms because the MPM particles do not penetrate the FEM body (conservation of mass). In addition, the continuity of the normal stress on the interface is automatically satisfied (conservation of momentum). The monolithic coupling proposed in this work is highly inspired by monolithic coupling strategies for fluid-structure interaction (FSI) problems [38–42]. As a matter of fact, the MPM background grid is used in the same way as the finite element grid employed to discretize the fluid domain in FSI problems. In such problems, the displacement of the fluid grid at the interface is required to match the displacement of the solid grid. The same requirement is enforced here between the MPM background grid and the FEM solid grid.

The weak system of equations solved in the coupled case is the following

$$\begin{aligned}
&\int_{\Omega_{ab}} \rho_{mpm}\left(\ddot{\boldsymbol{u}}_{mpm}\cdot\delta\boldsymbol{u}_{mpm} + \boldsymbol{\sigma}_{mpm}^{s} : \nabla\delta\boldsymbol{u}_{mpm} - \boldsymbol{b}_{mpm}\cdot\delta\boldsymbol{u}_{mpm}\right) dV\\
&-\int_{\Gamma_a} \rho_{mpm}\left(\boldsymbol{\sigma}_{mpm}^{s}\cdot\delta\boldsymbol{u}_{mpm}\right)\cdot\boldsymbol{n}_{mpm} = 0, \qquad \forall\delta\boldsymbol{u}_{mpm}\in\Delta U_{mpm},\\
&\int_{\Omega_{fem}} \rho_{fem}\ddot{\boldsymbol{u}}_{fem}\cdot\delta\boldsymbol{u}_{fem} + \boldsymbol{\sigma}_{fem} : \nabla\delta\boldsymbol{u}_{fem} - \rho_{fem}\boldsymbol{b}_{fem}\cdot\delta\boldsymbol{u}_{fem}\, dV\\
&-\int_{\Gamma_a}\left(\boldsymbol{\sigma}_{fem}\cdot\delta\boldsymbol{u}_{fem}\right)\cdot\boldsymbol{n}_{fem} = 0, \qquad \forall\delta\boldsymbol{u}_{fem}\in\Delta U_{fem},
\end{aligned} \tag{36}$$

where ΔU_{fem} represents the set of the test functions for the FEM weak formulation. Because two elastic bodies are simulated, the momentum equation is the same for both the MPM and the FEM body and the Cauchy stress is still given by Eq. (12) for both solids. Recall from Section 2.2 that $\Gamma_a = \partial\Omega_{ab}\cap\partial\Omega_{fem}$denotes the interface between the MPM and the FEM domains. The continuity of mass and momentum between the equations in system (36) are satisfied. Namely,

$$\boldsymbol{u}_{mpm} = \boldsymbol{u}_{fem}(\boldsymbol{\sigma}\cdot\boldsymbol{n})|_{fem,\Gamma_a} + (\boldsymbol{\sigma}\cdot\boldsymbol{n})|_{mpm,\Gamma_a} = 0, \tag{37}$$

where the second equation means that the FEM and the MPM values of $(\boldsymbol{\sigma}\cdot\boldsymbol{n})$ match on Γ_a. Due to the monolithic approach, the equations for the MPM body and for the FEM body are solved at the same time with a unique assembly for the two. The assembly procedure is carried out exactly in the same way as in Section 3.3 for the nodes on the MPM background grid $\mathcal{T}_b$. If $\mathcal{T}_{fem}$ denotes the finite element grid used to discretize Ω_{fem}, let $\mathcal{I}_{fem}$ be the set of grid points of $\mathcal{T}_{fem}$. The inactive grid contributions are given only to the nodes in $\mathcal{I}\setminus(\mathcal{I}_{ab}\cup\mathcal{I}_{fem})$, so no coupling between inactive nodes and FEM nodes exists. For any node in $\mathcal{I}_{fem}$, the assembly procedure is carried out in a standard finite element fashion, using Gauss points as quadrature points. Recalling the constitutive law in Eq. (12), for a given Gauss point i_g, we define σ_{ij,i_g}^{s} by

$$\boldsymbol{\sigma}_{i_g}^{s} := \frac{\lambda_{fem}\,\log\left(J_{i_g}\right)}{\rho_{fem}\,J_{i_g}}\boldsymbol{I} + \frac{\mu_{fem}}{J_{i_g}}\left(\boldsymbol{B}_{i_g} - \boldsymbol{I}\right), \tag{38}$$

where $J_{i_g} = \det(\boldsymbol{F}_{i_g})$, $\boldsymbol{B}_{i_g} = \boldsymbol{F}_{i_g}\left(\boldsymbol{F}_{i_g}\right)^{T}$ and

$$\boldsymbol{F}_{i_g} = \left(\widehat{\nabla}\boldsymbol{u}_{g}\left(\boldsymbol{x}_{i_g}\right) + \boldsymbol{I}\right). \tag{39}$$

In Eq. (39), $\widehat{\nabla}\boldsymbol{u}_{g}\left(\boldsymbol{x}_{i_g}\right)$ represents the background grid displacement gradient with respect to the undeformed finite element configuration, evaluated at $\boldsymbol{x}_{i_g}$, given by

$$\widehat{\nabla} u_{ij,g}\left(\boldsymbol{x}_{i_g}\right) := \sum_{I_\varepsilon=1}^{N_{\mathcal{E}_g}} u_{i,I_\varepsilon}\,\frac{\partial\widehat{\phi}_{I_\varepsilon}}{\partial\widehat{x}_j}\left(\boldsymbol{x}_{i_g}\right). \tag{40}$$

For any $\mathcal{E}\in\mathcal{T}_{fem}$, the local residual is

$$\begin{aligned}
r_{fem,i,I_\varepsilon} := \sum_{i_g=1}^{N_{\mathcal{E}_g}}\omega_{i_g}\Bigg[&\ddot{u}_{i,i_g}\,\phi_{I_\varepsilon}\left(\boldsymbol{x}_{i_g}\right) + \left(\sum_{j=1}^{d}\sigma_{ij,i_g}^{s}\,\frac{\partial\phi_{I_\varepsilon}}{\partial x_j}\left(\boldsymbol{x}_{i_g}\right)\right)\\
&-\frac{\rho_{fem}\,b_{i,i_g}}{J_{i_g}}\phi_{I_\varepsilon}\left(\boldsymbol{x}_{i_g}\right)\Bigg] = 0, \text{ for } I_\varepsilon = 1,\ldots,N_\varepsilon.
\end{aligned} \tag{41}$$

Because particles are replaced by Gauss points in the FEM assembly, the Newmark scheme in Eq. (19) for the FEM body becomes

$$\ddot{\boldsymbol{u}}_{i_g}^{n+1} = \frac{1}{\beta\,\Delta t^2}\left(\boldsymbol{u}_{i_g}^{n+1} - \boldsymbol{u}_{i_g}^{n}\right) - \frac{1}{\beta\Delta t}\,\dot{\boldsymbol{u}}_{i_g}^{n} - \frac{1-2\beta}{2\beta}\ddot{\boldsymbol{u}}_{i_g}^{n}, \tag{42}$$

where

$$\boldsymbol{u}_{i_g}^{n+1} = \boldsymbol{u}^{n+1}\left(\boldsymbol{x}_{i_g}\right) := \sum_{I_\varepsilon=1}^{N_{\mathcal{E}g}}\boldsymbol{u}_{I_\varepsilon}^{n+1}\,\phi_{I_\varepsilon}\left(\boldsymbol{x}_{i_g}\right). \tag{43}$$

The displacement, velocity and acceleration at the Gauss point at time t^n in Eq. (42) are computed in an analogous way as the displacement at the Gauss point at time t^{n+1} in Eq. (43). The coupled monolithic block system is again block diagonal and is given by

$$\begin{bmatrix}
\boldsymbol{K}_{ab}\left(\boldsymbol{u}^{k}\right) & \boldsymbol{K}_{ab,fem}\left(\boldsymbol{u}^{k}\right) & \boldsymbol{0}\\
\boldsymbol{K}_{fem,ab}\left(\boldsymbol{u}^{k}\right) & \boldsymbol{K}_{fem}\left(\boldsymbol{u}^{k}\right) & \boldsymbol{0}\\
\boldsymbol{0} & \boldsymbol{0} & \boldsymbol{M}_{ib}
\end{bmatrix}
\begin{bmatrix}
\Delta\boldsymbol{u}_{ab}^{k+1}\\ \Delta\boldsymbol{u}_{fem}^{k+1}\\ \Delta\boldsymbol{u}_{ib}^{k+1}
\end{bmatrix} =
\begin{bmatrix}
-\boldsymbol{r}_{ab}\left(\boldsymbol{u}^{k}\right)\\ -\boldsymbol{r}_{fem}\left(\boldsymbol{u}^{k}\right)\\ -\boldsymbol{r}_{ib}\left(\boldsymbol{u}^{k}\right)
\end{bmatrix}, \tag{44}$$

where

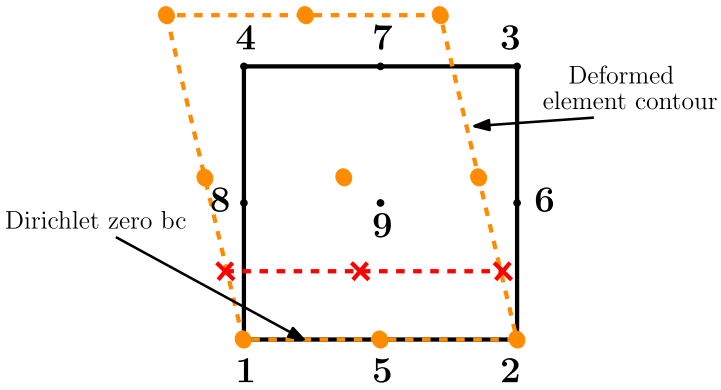

Fig. 4. Schematics for the receding contact force algorithm.

$$
\begin{aligned}
&\boldsymbol{K}_{ab}\left(\boldsymbol{u}^k\right) := \boldsymbol{K}_{soft}\left(\boldsymbol{u}^k\right) + \boldsymbol{K}_{mpm}\left(\boldsymbol{u}^k\right),\\
&\boldsymbol{r}_{ab}\left(\boldsymbol{u}^k\right) := \boldsymbol{r}_{soft}\left(\boldsymbol{u}^k\right) + \boldsymbol{r}_{mpm}\left(\boldsymbol{u}^k\right),\\
&\boldsymbol{K}_{soft}\left(\boldsymbol{u}^k\right) := \frac{\partial \boldsymbol{r}_{soft}\left(\boldsymbol{u}^k\right)}{\partial \boldsymbol{u}_{ab}}, \quad \boldsymbol{K}_{mpm}\left(\boldsymbol{u}^k\right) := \frac{\partial \boldsymbol{r}_{mpm}\left(\boldsymbol{u}^k\right)}{\partial \boldsymbol{u}_{ab}},\\
&\boldsymbol{K}_{ab,fem}\left(\boldsymbol{u}^k\right) := \frac{\partial \boldsymbol{r}_{ab}\left(\boldsymbol{u}^k\right)}{\partial \boldsymbol{u}_{fem}}, \quad \boldsymbol{K}_{fem,ab}\left(\boldsymbol{u}^k\right) := \frac{\partial \boldsymbol{r}_{fem}\left(\boldsymbol{u}^k\right)}{\partial \boldsymbol{u}_{ab}},\\
&\boldsymbol{r}_{ib}\left(\boldsymbol{u}^k\right) := \boldsymbol{r}_{mass}\left(\boldsymbol{u}^k\right), \quad \boldsymbol{M}_{ib} := \frac{\partial \boldsymbol{r}_{mass}\left(\boldsymbol{u}^k\right)}{\partial \boldsymbol{u}_{ib}}.
\end{aligned}
\tag{45}
$$

The (1,2) and (2,1) blocks represent the coupling between the active background grid and the FEM body nodes. After the solution of the monolithic system, the nodal values of velocity and acceleration at the grid nodes in $\mathcal{I}_{fem}$ are updated using the Newmark scheme

$$
\begin{aligned}
&\ddot{\boldsymbol{u}}_I^{n+1} = \tfrac{1}{\beta\Delta t^2}\left(\boldsymbol{u}_I^{n+1} - \boldsymbol{u}_I^n\right) - \tfrac{1}{\beta\Delta t}\dot{\boldsymbol{u}}_I^n - \tfrac{1-2\beta}{2\beta}\ddot{\boldsymbol{u}}_I^n,\\
&\dot{\boldsymbol{u}}_I^{n+1} = \dot{\boldsymbol{u}}_I^n + \Delta t\left((1-\gamma)\ddot{\boldsymbol{u}}_I^n + \gamma\,\ddot{\boldsymbol{u}}_I^{n+1}\right).
\end{aligned}
\tag{46}
$$

5. Receding contact force correction

The MPM domain may be subject to roto-translation and large deformations, and it is possible for its boundary to come into contact with a domain boundary where a Dirichlet boundary condition is imposed, or with the FEM solid boundary. These situations require the contact force modeling to be carefully described. The contact force between two surfaces acts only when they touch, and a mutual pressure is applied. During the receding phase, when the bodies detach, the contact force must be zero. Moreover, compenetration between the touching domains should never occur. The proposed monolithic formulation never allows for compenetration, and the force balance at the interface is automatically satisfied in the touching phase of the contact. However, in the receding phase, the contact suffers of small to moderate *sticky* effects, that grow with increasing values of the Young's modulus of the MPM body.

To avoid the artificial stickiness in the receding phase, a simple correction to the contact description is embedded in the implicit monolithic formulation. This correction requires a small modification in the MPM assembly for those elements of the active background grid for which a face is shared with an element of the FEM body, or Dirichlet boundary conditions are imposed on it. The nodal displacement values of such elements receive an additional contribution for each enclosed particle that moves away from the face. The idea is to reduce the reaction force exerted by the face in the evaluation of $\boldsymbol{F}_p$ in Eq. (24). In particular, a reduction of the contribution of $\widetilde{\nabla}\widetilde{\boldsymbol{u}}_g(\boldsymbol{x}_p)$ to the deformation gradient $\boldsymbol{F}_p$ is obtained. The algorithm has been implemented here only for biquadratic Lagrangian quadrilateral elements but it readily extends to other shapes and families of finite elements. Let p be a particle and let $\mathcal{E}_p$ be the element that encloses it, depicted in Fig. 4. For simplicity, we consider the case where Dirichlet zero boundary conditions have been imposed on the lower face of $\mathcal{E}_p$. Hence, the lower face will remain undeformed in the time interval $(t^n, t^{n+1}]$. This implies that $\widetilde{\boldsymbol{u}}_1 = \widetilde{\boldsymbol{u}}_2 = \widetilde{\boldsymbol{u}}_5 = \boldsymbol{0}$, whereas the other nodes are free to move, see the dashed contour in Fig. 4. If the particle moves away from the Dirichlet boundary, the values of $\widetilde{\boldsymbol{u}}_{I_{\mathcal{E}_p}}$, with $I_{\mathcal{E}_p} = 1, \ldots, N_{\mathcal{E}_p} = 9$, are modified as follows

$$
\begin{aligned}
&\widetilde{\boldsymbol{u}}_1^* = (1-C_c)\widetilde{\boldsymbol{u}}_1 + C_c\left(\tfrac{4}{3}\widetilde{\boldsymbol{u}}_4 - \tfrac{1}{3}\widetilde{\boldsymbol{u}}_8\right),\\
&\widetilde{\boldsymbol{u}}_2^* = (1-C_c)\widetilde{\boldsymbol{u}}_2 + C_c\left(\tfrac{4}{3}\widetilde{\boldsymbol{u}}_3 - \tfrac{1}{3}\widetilde{\boldsymbol{u}}_6\right),\\
&\widetilde{\boldsymbol{u}}_5^* = (1-C_c)\widetilde{\boldsymbol{u}}_5 + C_c\left(\tfrac{4}{3}\widetilde{\boldsymbol{u}}_7 - \tfrac{1}{3}\widetilde{\boldsymbol{u}}_9\right),\\
&\widetilde{\boldsymbol{u}}_{I_{\mathcal{E}_p}}^* = \widetilde{\boldsymbol{u}}_{I_{\mathcal{E}_p}} \text{ for } I_{\mathcal{E}_p} = 3,4,6,7,8,9,
\end{aligned}
\tag{47}
$$

with $C_c \in [0,1]$. The terms multiplied by C_c in the above equations represent the correction terms. The new deformation field allows the nodes on the lower face to move, see the red dashed line with the crosses in Fig. 4. The crosses represent the positions of the nodes 1, 5 and 2, subject to this new deformation field. For $C_c = 0$, the Dirichlet boundary condition is restored. For $C_c = 1$, the new displacement field is such that $\widetilde{\nabla}\widetilde{\boldsymbol{u}}_g^*(\boldsymbol{x}_1) = \widetilde{\nabla}\widetilde{\boldsymbol{u}}_g^*(\boldsymbol{x}_2) = \widetilde{\nabla}\widetilde{\boldsymbol{u}}_g^*(\boldsymbol{x}_5) = \boldsymbol{0}$, and consequently for each particle p located on the lower face it would be

$$
\boldsymbol{F}_p = \left(\widetilde{\nabla}\widetilde{\boldsymbol{u}}_g^*(\boldsymbol{x}_p) + \boldsymbol{I}\right)\boldsymbol{F}_p^n = \boldsymbol{F}_p^n,
\tag{48}
$$

with no new contribution to the stress tensor. For $C_c \in (0,1)$, the resulting boundary condition can be considered of mixed type. The equations in (47) can be used also for the case of non zero Dirichlet boundary condition or contact of the MPM body with the FEM body.

The value of the constant C_c has been investigated numerically in the next section.

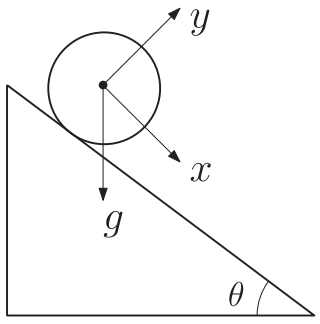

Fig. 5. Schematics of the rolling disk test.

6. Numerical results

First, the implicit MPM scheme is tested, followed by the monolithic coupling between MPM and FEM. When possible, the numerical results are compared to analytic solutions to highlight the great accuracy of the methods presented. For simplicity, only 2-dimensional numerical tests are performed, even if the methods developed in this work can be applied to 3-dimensional problems as well.

6.1. Initialization of the MPM bodies

In the numerical examples in Sections 6.2 and 6.3, two MPM bodies are considered: a disk and a beam. Both bodies have a uniform particle distribution in their core and a progressively refined distribution moving from an a priori chosen interior surface towards the boundary. Recall that the particle mass is defined as $m_p = \rho_0 V_p$, where ρ_0 is the initial density of the MPM body and V_p is the particle volume. This volume has a value that depends on the location of the particle within the particle distribution used to discretized the body. Two different initialization procedures are carried out depending on the specific body, as explained next.

6.1.1. Initialization of the disk

The input parameters for the disk are: the coordinates of the center of the disk (x_c, y_c), the radius of the disk R, the radius of the interior disk in which the uniform distribution is built R_0, and N_{θ_0}, which is the number of particles located within the disk of radius R_0. The number of boundary layers N_b between the circles can be obtained after R, R_0, and N_{θ_0} have been chosen. For each particle, the output parameters are its initial coordinates and its volume V_p.

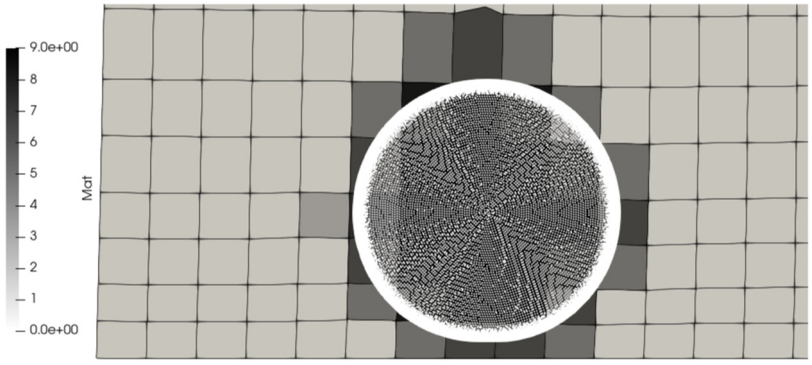

Fig. 6. Rolling disk simulation for $E = E_1 = 4.2 \cdot 10^6$ Pa. The different shades of gray for the elements of the background grid identify different values of M_ε, which is referred to as Mat in the legend. One refinement ($J = 1$) has been considered for the background grid.

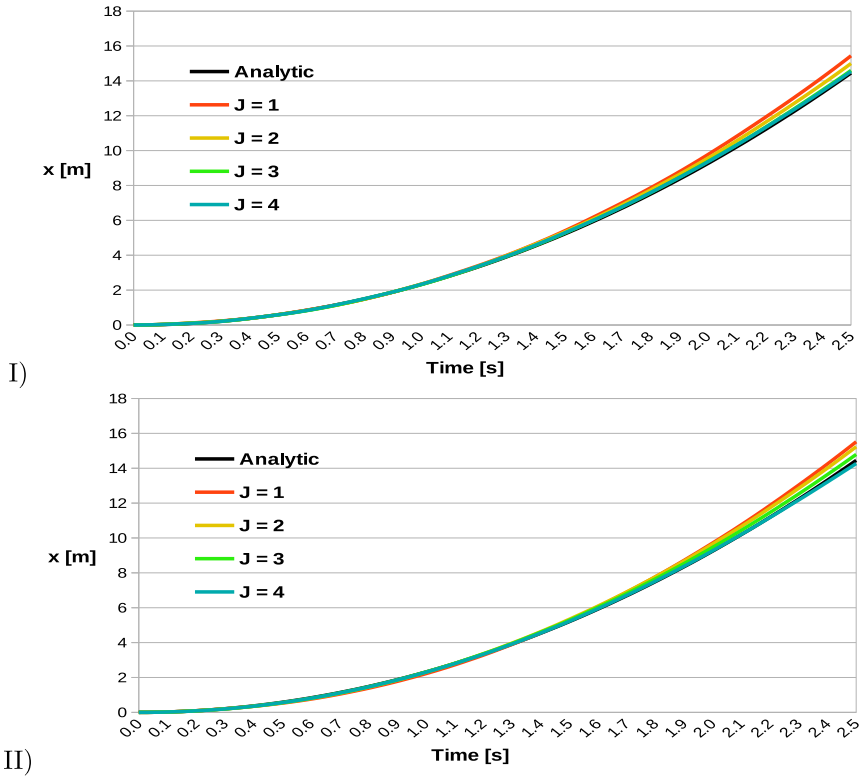

Fig. 7. Position of the center of mass of the rolling disk. (I): $E = E_1 = 4.2 \cdot 10^6$ Pa. (II): $E = E_2 = 4.2 \cdot 10^8$ Pa.

Table 1
Averaged relative error associated with the results in Fig. 7.

E	$C_\mathcal{E}$	$J=1$	$J=2$	$J=3$	$J=4$
$4.2 \cdot 10^6$	Eq. (50)	$5.545 \cdot 10^2$	$3.921 \cdot 10^2$	$2.571 \cdot 10^2$	$2.253 \cdot 10^2$
$4.2 \cdot 10^8$	Eq. (51)	$4.520 \cdot 10^2$	$3.502 \cdot 10^2$	$2.423 \cdot 10^2$	$1.720 \cdot 10^2$

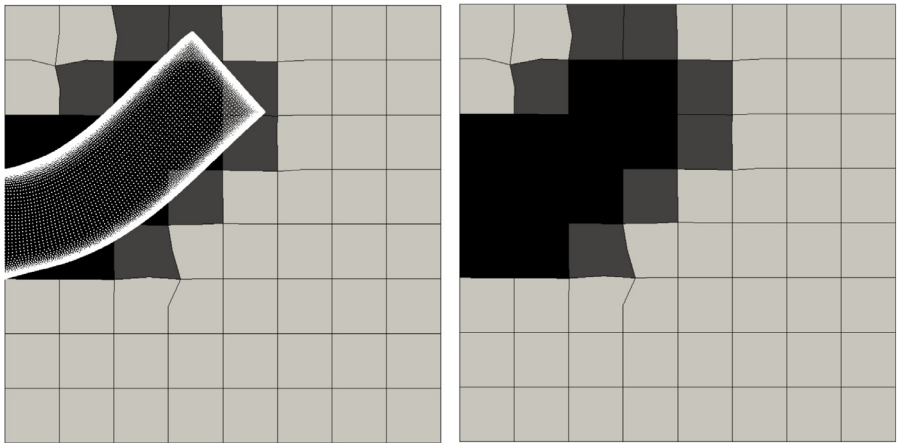

Fig. 8. Cantilever beam simulation with $J = 2$. The MPM particles are omitted on the right figure to highlight the deformations and the values of M_ε for the background grid elements.

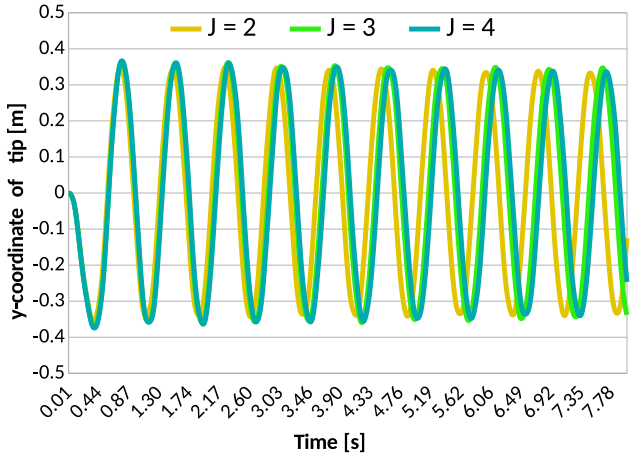

Fig. 9. Oscillations of the tip of the cantilever beam, as the resolution of the background grid is varied.

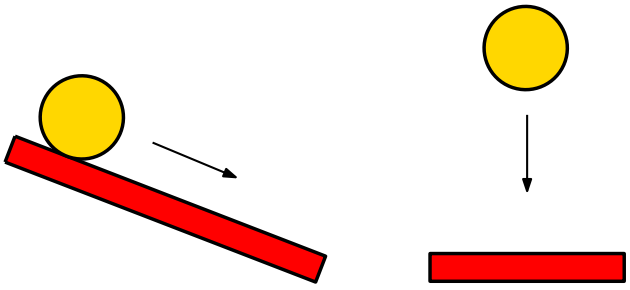

Fig. 10. Schematics of the MPM-FEM coupling tests considered. Disk rolling on an inclined plate (left) and disk bouncing on a plate (right). The MPM disk is in light color whereas the FEM plate is in dark color. (For interpretation of the references to colour in this figure legend, the reader is referred to the web version of this article.)

6.1.2. Initialization of the beam

The input parameters for the beam are: the coordinates of the midpoint of the left boundary (x_0, y_0), the height H and length L of the beam, the height H_0 of the interior beam in which a uniform distribution is built, and the number N_H of particle rows in the interior beam. The number of boundary layers N_b between the beams can be obtained once H, H_0 and N_H are chosen. For each particle, the output parameters are again its initial coordinates and its volume V_p.

The pseudocode for the initialization of the two MPM bodies is given in Appendix A. We remark that the performances of the method do not depend on the specific particle distribution adopted and other distributions may be possible.

6.2. Tests for the implicit MPM

We begin by considering a 2-dimensional example of a disk rolling on an inclined plane. The case of a rolling disk (or ball in 3D) is a common test for the MPM, and it has been used in several other works, we report for instance [8,29,28]. The plane has an inclination of $\theta = \pi/4$, the disk has radius $R = 1.6$ m, and Young's modulus E. Two values of E are chosen for the simulations, $E_1 = 4.2 \cdot 10^6$ Pa and $E_2 = 4.2 \cdot 10^8$ Pa. The coarse mesh is composed of 4 horizontal layers, each with 20 bi-quadratic quadrilateral elements, and each of them has unitary length in the x-direction. Because the mesh is progressively refined moving towards the plane, each layer has a different cell size in the y-direction. These lengths are 1.72 m, 1.34 m, 1.09 m, and 0.85 m. Finer grids are obtained with midpoint refinement. Hence, after every refinement, the number of elements increases by a factor of four. Let J denote the number of refinements carried out for a given simulation. For instance, if $J = 3$, the coarse background grid is refined 3 times. If $J = 0$, it means that the coarse grid is not refined. The values of $J = 1,\ 2,\ 3,\ 4$ are chosen for the tests. The initial distance $d_0(J)$ of the center of the disk from the plane depends on the refinement of the grid, and it is designed to keep a small gap between the disk and the plane. For given J and E, the gap is a fraction of the height of the element of the background grid where the contact occurs. We choose $d_0(J) = R + 0.2/2^{J-1}$ for

E_1, and $d_0(J) = R + 0.3/2^{J-1}$ for E_2. The reference frame is translated and centered at the center of the disk as in Fig. 5. The analytic expression of the x-coordinate of the center of mass assuming an undeformable disk is given by

$$x(t) = x_0 + \frac{1}{3} g t^2 \sin(\theta), \tag{49}$$

where x_0 is assumed to be zero. Concerning the other simulation parameters, the density of the disk is 1000 kg/m^3, the Poisson's coefficient is $\nu = 0.4$, and the step size is $\Delta t = 0.01$ s. For Newmark's integrator, $\beta = 0.3$ and $\gamma = 0.5$ are selected. Rolling without slip is considered and $C_c = 0.5$. The input parameters for the generation of the disk are $(x_c, y_c) = (0, 0), R_0 = 1.4$ m$, R = 1.6$ m$, N_{\theta_0} = 300$, and $N_b = 22$, for a total of 48,739 particles.

In Fig. 6, the particle distribution (including the particle boundary layers) and some details about the graded mesh for the background grid are visible. In the same figure the values of the flags M_ε are also reported for the elements of the background grid.

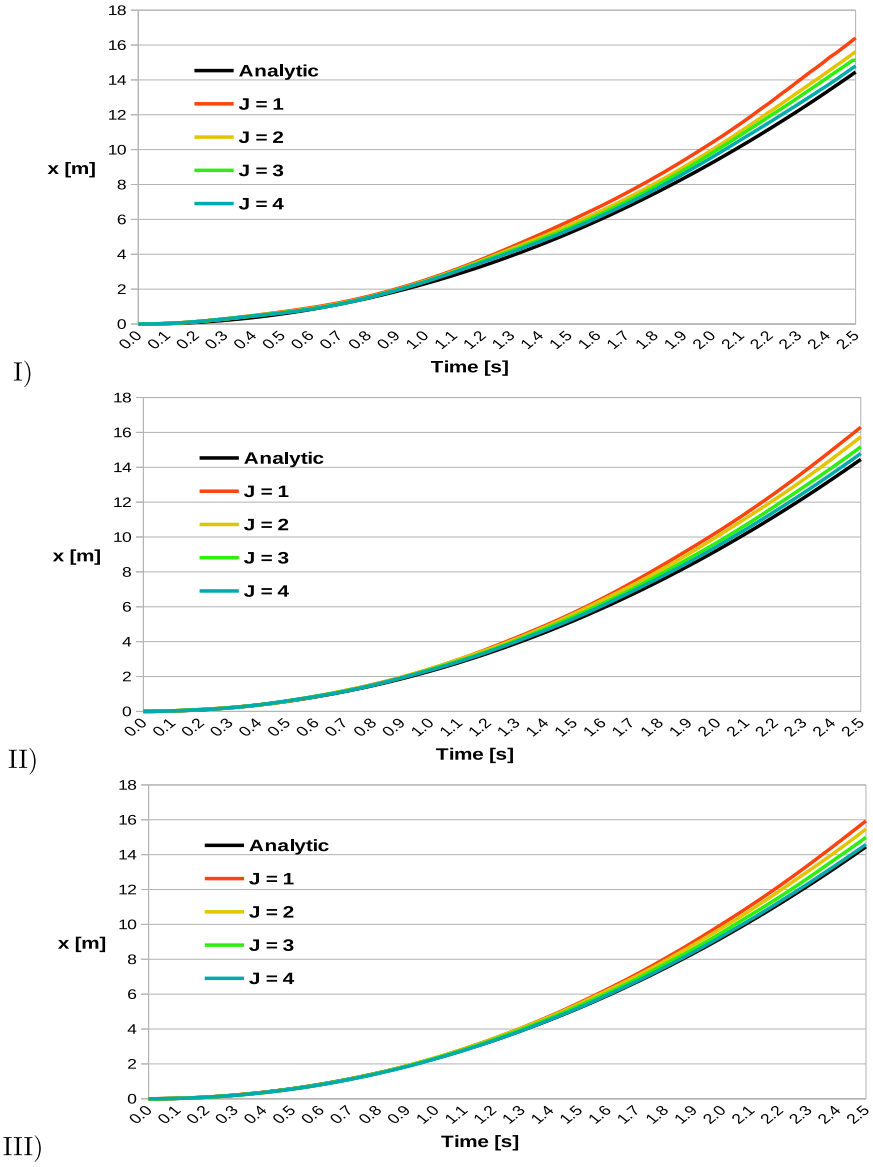

Fig. 11. Position of the center of mass of the rolling disk for the coupled MPM-FEM case. (I): $E_{mpm} = 4.2 \cdot 10^6$ Pa and $E_{fem} = 8.4 \cdot 10^6$ Pa. (II): $E_{mpm} = 4.2 \cdot 10^7$ Pa and $E_{fem} = 8.4 \cdot 10^7$ Pa. (III): $E_{mpm} = 4.2 \cdot 10^8$ Pa and $E_{fem} = 8.4 \cdot 10^8$ Pa.

Table 2
Averaged relative error associated with the results in Fig. 11.

E_{mpm}	E_{fem}	C_ε	$J = 1$	$J = 2$	$J = 3$	$J = 4$
$4.2 \cdot 10^5$	$8.4 \cdot 10^5$	Eq. (54)	$1.604 \cdot 10^1$	$1.263 \cdot 10^1$	$1.051 \cdot 10^1$	$8.783 \cdot 10^2$
$4.2 \cdot 10^6$	$8.4 \cdot 10^6$	Eq. (55)	$9.029 \cdot 10^2$	$7.918 \cdot 10^2$	$5.416 \cdot 10^2$	$3.654 \cdot 10^2$
$4.2 \cdot 10^7$	$8.4 \cdot 10^7$	Eq. (56)	$5.368 \cdot 10^2$	$4.289 \cdot 10^2$	$2.919 \cdot 10^2$	$1.959 \cdot 10^2$

Recall that because bi-quadratic elements are considered, the maximum possible value of M_ε is 9, which is attained for interior elements. The lightest gray refers to the elements of the inactive background grid. The following values were chosen for the soft stiffness scaling factor C_ε in Eq. (26)

$$\text{For } E_1: \; C_\varepsilon = \begin{cases} 10^{-3} & \text{if} \quad M_\varepsilon < 5, \\ 10^{-7} & \text{if} \quad 5 \leqslant M_\varepsilon < 9, \\ 0 & \text{if} \quad M_\varepsilon = 9, \end{cases} \tag{50}$$

$$\text{For } E_2: \; C_\varepsilon = \begin{cases} 10^{-5} & \text{if} \quad M_\varepsilon < 5, \\ 10^{-9} & \text{if} \quad 5 \leqslant M_\varepsilon < 9, \\ 0 & \text{if} \quad M_\varepsilon = 9. \end{cases} \tag{51}$$

The horizontal position of the center of mass obtained numerically solving our implicit MPM scheme is compared to the analytic expression in Eq. (49) for different values of J, and E. Results for E_1 are visible in Fig. 7(I), for different mesh sizes. The curves obtained with the proposed implicit MPM method are in agreement with the analytic equation of the center of mass in Eq. (49). It is also shown that a progressive refinement of the mesh provides increasingly accurate results, because the curve associated with $J = 4$ is the one that best overlaps with the analytic expression. The curve for $J = 3$ overlaps with that of $J = 4$, this is why it is hardly visible in the figure. Results for E_2 are reported in Fig. 7(II). Once again, the curves are in agreement with the analytic expression and larger values of J give better accuracy.

Average relative errors are also shown, to provide a quantitative measure of the error. If $x(t)$ represents the position of the center of mass defined in Eq. (49), let $\bar{x}(t)$ be the position computed with the proposed method. Then the averaged relative error is defined as

$$\frac{1}{N_t}\sum_{i=1}^{N_t} \frac{|x(t_i) - \bar{x}(t_i)|}{x(t_i)}, \tag{52}$$

where $N_t = 250$ is the total number of time steps considered. Results for the above error are reported in Table 1 corresponding to the curves in Fig. 7.

The section continues with simulations of a cantilever beam with length $L = 0.625$ m and height $H = 0.25$ m, visible in Fig. 8. The parameters to build the MPM beam are $(x_0, y_0) = (0, 0), L, H, H_0 = 0.15\text{ m}, N_H = 20$, and $N_b = 21$, for a total of 23,041 particles. The domain is a unit box, whose midpoint of the left boundary is placed at the origin, and the coarse mesh is composed of 4 bi-quadratic quadrilateral elements. The background grid obtained when $J = 2$ is visible in Fig. 8. The beam has density $\rho = 10,000\,\text{kg/m}^3$, Poisson's coefficient $\nu = 0.4$, and Young's modulus $E = 1.74 \cdot 10^6$ Pa. These mechanical parameters have been chosen to observe a sufficient oscillation of the beam. The step size is $\Delta t = 0.008$ s and, as before, $\beta = 0.3$ and $\gamma = 0.5$ are chosen for Newmark's integrator. The values of C_ε are

$$C_\varepsilon = \begin{cases} 10^{-6} & \text{if} \quad M_\varepsilon < 5, \\ 10^{-10} & \text{if} \quad 5 \leqslant M_\varepsilon < 9, \\ 0 & \text{if} \quad M_\varepsilon = 9. \end{cases} \tag{53}$$

The beam is initially subject to its self weight, so only the gravitational force is applied to it. Then, when it reaches its larges deformation, is assumed that the gravitational force is removed and the oscillations of the tip of the beam are monitored. If no significant damping in the oscillations can be observed as time increases, it means that the method is accurate. Graphs for such oscillations are reported in Fig. 9, for values of $J = 2$, $J = 3$ and $J = 4$. From Fig. 9 it can be seen that, as time increases, the oscillations became slightly off-phase as the mesh becomes finer. Nevertheless, the damping of the oscillations is very small for all mesh sizes considered, despite the long duration of the simulation which is 8 seconds.

6.3. Tests for the MPM-FEM coupling

Numerical results for the MPM-FEM coupling are presented here. We begin by considering a disk rolling on an inclined plate, as in [28,29]. Please see Fig. 10 for schematics of this layout. The disk is modeled with MPM whereas the plate is discretized with FEM. The dimensions of the plate are 20×1.6 m while the radius of the disk is $R = 1.6$ m. Rolling without slip is considered and the inclination of the plate is $\theta = \pi/4$. The MPM background grid is the same as the one used for the rolling ball in the uncoupled case, whereas for the FEM plate two horizontal layers of 20 elements each are considered, with x length 1 m and y length 0.85 m. Recall that the use of a background grid for the MPM attached to the FEM body is one of the major contributions of

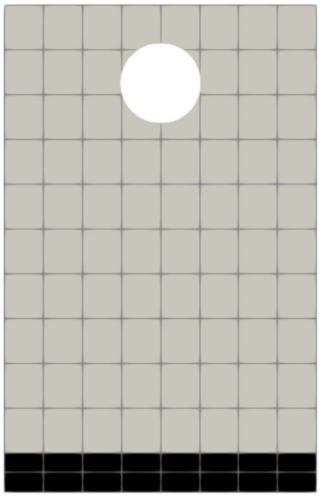

Fig. 12. Disk falling on a horizontal plate.

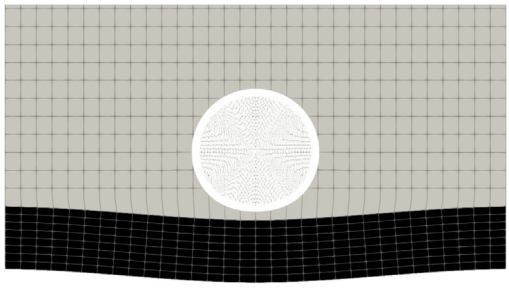

Fig. 13. Deformation of the disk and plate as the disk impacts on the plate.

Table 3
Contact constant C_c and step size near the plate Δt_{plate} for the bouncing disk case.

	$J = 2$	$J = 3$	$J = 4$
	C_c		
$C_{\varepsilon,1}$	0.06	0.1	0.2
$C_{\varepsilon,2}$	0	0.1	0.2
	Δt_{plate} [s]		
$C_{\varepsilon,1}$	0.0005	0.00025	0.000125
$C_{\varepsilon,2}$	0.001	0.0005	0.00025

the present work. The coupling coefficient C_c is equal to 0.5. The coarse grid is refined by means of midpoint refinement, with J indicating the number of refinements performed. The density and the Poisson's coefficient of both the disk and the plate are set to 1000 kg/m^3 and $\nu = 0.4$, respectively. For the time integration, $\Delta t = 0.01$ s, and the parameters for Newmark's integrator are $\beta = 0.3$ and $\gamma = 0.5$. The Young's moduli of the MPM and the FEM bodies are respectively $E_{mpm} = 4.2 \cdot 10^{\alpha}$ Pa and $E_{fem} = 8.4 \cdot 10^{\alpha}$ Pa, with $\alpha = 6, 7, 8$. These values are not chosen to represent any specific material. The initial vertical distance $d_0(J)$ of the center of the disk from the plane is $d_0(J) = R + 0.15/2^{J-1}$ for $\alpha = 6$, $d_0(J) = R + 0.2/2^{J-1}$ for $\alpha = 7$, and $d_0(J) = R + 0.25/2^{J-1}$ for $\alpha = 8$. With these definitions, there exists an initial small gap between the disk and the plate, and the gap dimension is a fraction of the height of the background grid element where the contact occurs. The reference frame is then translated and centered at the center of mass of the disk, hence the analytic expression of the x-coordinate of the center of mass is given in Eq. (49). The parameters for the initialization of the MPM disk are $(x_c, y_c) = (0, 0)$, $R = 0.16$ m, $R_0 = 0.14$ m, $N_{\theta_0} = 600$ and $N_b = 24$, for a total of 57,084 particles. The coefficients C_ε for the present tests are as follows:

$$\text{for } \alpha = 6: \; C_\varepsilon = \begin{cases} 10^{-2} & \text{if} \quad M_\varepsilon < 5, \\ 10^{-6} & \text{if} \quad 5 \leqslant M_\varepsilon < 9, \\ 0 & \text{if} \quad M_\varepsilon = 9, \end{cases} \tag{54}$$

$$\text{for } \alpha = 7: \; C_\varepsilon = \begin{cases} 10^{-3} & \text{if} \quad M_\varepsilon < 5, \\ 10^{-7} & \text{if} \quad 5 \leqslant M_\varepsilon < 9, \\ 0 & \text{if} \quad M_\varepsilon = 9. \end{cases} \tag{55}$$

$$\text{for } \alpha = 8: \; C_\varepsilon = \begin{cases} 10^{-4} & \text{if} \quad M_\varepsilon < 5, \\ 10^{-8} & \text{if} \quad 5 \leqslant M_\varepsilon < 9, \\ 0 & \text{if} \quad M_\varepsilon = 9. \end{cases} \tag{56}$$

In Fig. 11, results are displayed for $\alpha = 6,\ 7,\ 8$. We observe that also in the coupled case there is agreement between the numerical results and the analytic position of the center of mass. Increasing values of J provide better accuracy with respect to the analytic curve. Moreover, to stiffer materials it corresponds a smaller error. This is also expected because the analytic solution is obtained under the assumption of an undeformable body. The averaged relative errors reported in Table 2 confirm the accuracy and validity of the proposed coupling method. This section is concluded with simulations of a disk falling from above and bouncing on a horizontal plate. For schematics of this layout, please see Fig. 10. As before, the disk is modeled with MPM and the plate is discretized with FEM. The coarse MPM background grid has dimensions 1.28×1.84 m and it is made of 80 elements of x length 0.16 m and y length 0.184 m. The FEM plate has dimensions 1.28×0.64 m and is discretized with 2 horizontal layers of 8 cells each, of x length 0.16 m and y length 0.08 m. The disk has radius $R = 0.16$ m and is placed initially at the center-top of the

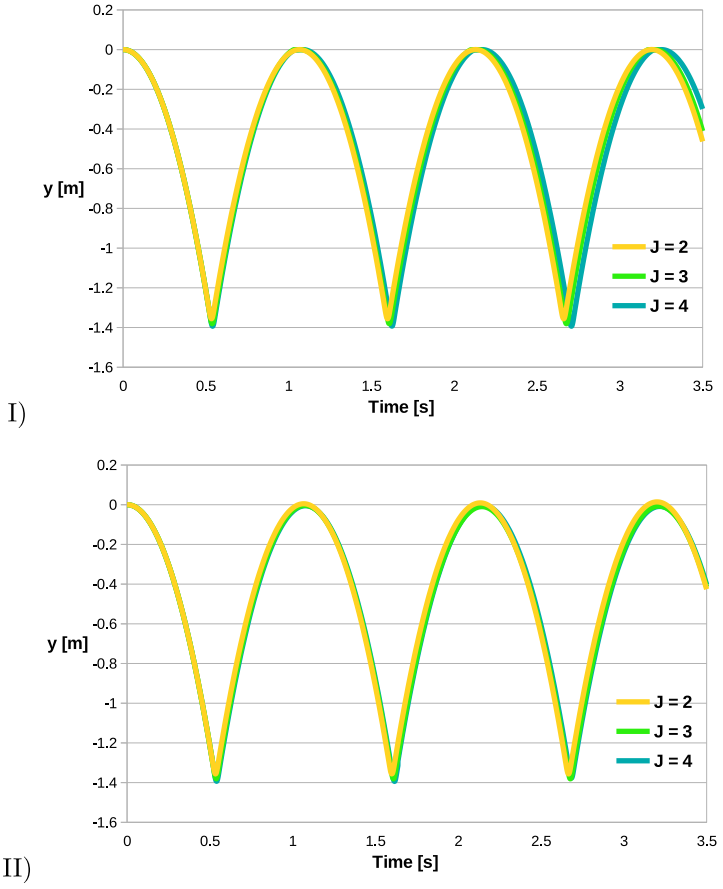

Fig. 14. Vertical position of the center of mass of a disk bouncing on a plate. (I) $C_\varepsilon = C_{\varepsilon,1}$ defined in Eq. (57). (II) $C_\varepsilon = C_{\varepsilon,2}$ defined in Eq. (58).

background grid such that its distance from the upper surface of the plate is 1.68 m. The coarse background grid and the MPM discretization are visible in Fig. 12, whereas a picture of the impact between the disk and the plate can be found in Fig. 13.

The parameters for the initialization of the MPM disk are now $(x_c, y_c) = (0, 0)$, $R = 0.16\,\text{m}, R_0 = 0.14\,\text{m}, N_{\theta_0} = 300$ and $N_b = 22$, for a total of 48,739 particles. Both the disk and the plate have density $\rho_{mpm} = \rho_{fem} = 1000\,\text{kg/m}^3$ and Poisson's coefficient $\nu = 0.4$. The Young's moduli for the MPM and FEM body are, respectively, $E_{mpm} = 5.91 \cdot 10^6$ Pa and $E_{fem} = 4.2 \cdot 10^7$ Pa. The aim of these tests is to further demonstrate the accuracy of the proposed methods and to highlight how it improves as the values of the coefficient C_ε is decreased, considering fixed values of E. This behavior is explained by the fact that for fixed Young's modulus, smaller values of C_ε decrease the soft stiffness contribution and therefore decrease the error added to the method. The values of C_ε for this example are as follows

$$C_{\varepsilon,1} = \begin{cases} 10^{-2} & \text{if} \quad M_\varepsilon < 5, \\ 10^{-6} & \text{if} \quad 5 \leqslant M_\varepsilon < 9, \\ 0 & \text{if} \quad M_\varepsilon = 9, \end{cases} \tag{57}$$

$$C_{\varepsilon,2} = \begin{cases} 10^{-5} & \text{if} \quad M_\varepsilon < 5, \\ 10^{-9} & \text{if} \quad 5 \leqslant M_\varepsilon < 9, \\ 0 & \text{if} \quad M_\varepsilon = 9. \end{cases} \tag{58}$$

The value of the coupling coefficient C_c in this case depends on the refinement level and on C_ε. Its values are reported in Table 3. To speed up the simulation, the time stepping is adaptive, meaning that Δt is large when the disk is far from the plate and it is suddenly decreased after the disk reaches a given distance from the plate. The value of Δt when the disk is near the plate is reported in Table 3. The parameters for Newmark's integrator are once again $\beta = 0.3$ and $\gamma = 0.5$.

The results for $C_{\varepsilon,1}$ are displayed in Fig. 14 I), where the vertical position of the center of mass is tracked as time increases. It is assumed that the reference frame is positioned on the initial position of the center of mass and that the plate is not subject to the gravitational force, to avoid oscillations not caused by the impact. As the refinement of the background grid increases, a slight offset between the curves is observed, the magnitude of which increases with time. An analogous situation was observed in Fig. 9, for the case of an oscillating cantilever beam. A different situation occurs for $C_{\varepsilon,2}$, displayed in Fig. 14(II): comparing this figure to Fig. 14(I), it can be seen that the offset is considerably reduced and now all the curves are in better agreement, especially those for $J = 3$ and $J = 4$. In both examples, no damping of the oscillations is observed, confirming once again the reliability and accuracy of our monolithic coupling. The results presented here show that, for fixed values of the Young's modulus, it is important for the accuracy of the simulation to choose the least possible values of C_ε that guarantees convergence.

7. Conclusion

A new coupling procedure for the interaction of an MPM body with a FEM body has been presented. The novelty consists of a monolithic approach that treats the two bodies as a single continuum, eliminating the need for contact search and detection algorithms. The proposed coupling has been tested on several numerical examples with a particular focus on accuracy and reliability. Results have shown that smaller errors are obtained with a progressive refinement of the MPM background grid, proving the consistency of the proposed strategy. We also investigated numerically the magnitude of the stiffness matrix contributions for a fixed value of the Young's modulus and confirmed the importance of an appropriate balance between stability and accuracy to have well performing simulations. This preliminary study has shown potential of the proposed coupling approach,and further work will be done in the future to fully explore its capabilities. For instance, different types of couplings other than solid-solid will be investigated, as well as techniques to use our monolithic approach for the coupling of the MPM with a fluid-structure interaction framework. This would pave the way for the use of our methodology on many applications of interest that go beyond the proof of concept examples shown in this work.

Appendix A

A.1. Initialization of the MPM disk pseudocode

Input Parameters: $x_c, y_c, R, R_0, N_{\theta_0}, N_b$ $\left(\text{with } N_b \geqslant \frac{R-R_0}{R_0}\text{ceil}\left(\frac{N_{\theta_0}}{2\pi}\right)\right)$

$N_r = \text{ceil}\left(\frac{N_{\theta_0}}{2\pi}\right), \quad \Delta R = \frac{R_0}{N_r}$

#Uniform Distribution

$p = 1, \quad x_p = x_c, \quad y_p = y_c$

for $i = 0, \ldots, N_r - 1$

$r_i = R_0 - i\Delta R, \quad N_{\theta_i} = \text{ceil}\left(N_{\theta_0}\frac{r_i}{R_0}\right), \quad \Delta\theta_i = \frac{2\pi}{N_{\theta_i}}$

for $j = 0, \ldots, N_{\theta_i} - 1$

$p = p + 1, \quad x_p = x_c + r_i\cos(j\Delta\theta_i), \quad y_p = y_c + r_i\sin(j\Delta\theta_i)$

end for

end for

for $i = 1, \ldots, p$

$m_p = \rho_{mpm}\frac{\pi R_0^2}{p}$

end for

#BoundaryLayers

Find a **such that** $\sum_{k=1}^{N_b}\Delta R a^k = R - R_0$

for $i = 1, \ldots, N_b$

$r_i = R_0 + \sum_{k=1}^{i}\Delta R a^k, \quad N_{\theta_i} = \text{ceil}\left(\frac{N_{\theta_0}}{a^i}\right), \quad \Delta\theta_i = \frac{2\pi}{N_{\theta_i}}$

for $j = 0, \ldots, N_{\theta_i} - 1$

$p = p + 1, \quad x_p = x_c + r_i\cos(j\Delta\theta_i), \quad y_p = y_c + r_i\sin(j\Delta\theta_i)$

$m_p = \rho_{mpm} r_i \Delta\theta_i \Delta R a^i$

end for

end for

A.2. Initialization of the MPM beam pseudocode

Input Parameters: $x_0, y_0, H, L, H_0, N_H, N_b \left(\text{with } N_b \geqslant \frac{H-H_0}{2}\frac{N_H-1}{H_0}\right)$

$\Delta H = \frac{H_0}{N_H-1},\ L_0 = L - \frac{H-H_0}{2},\ N_L = \text{ceil}\left(\frac{L_0}{\Delta H}\right),\ \Delta L = \frac{L_0}{N_L-1}$

#Uniform Distribution

$p = 1$

for $i = 0,\dots,N_L-1$

  for $j = 0,\dots,N_H-1$

    $p = p+1,\ x_p = x_0 + i\Delta L,\ y_p = y_0 - \frac{H_0}{2} + j\Delta H$

    $m_p = \rho_0 \Delta L \Delta H$

  end for

end for

#Boundary Layers

Find a **such that** $\sum_{k=1}^{N_b} \Delta H a^k = \frac{H-H_0}{2}$

for $i = 1,\dots,N_b$

  $H_i = H_0 + 2\sum_{k=1}^{i} \Delta H a^k,\ N_{H_i} = \text{ceil}\left(\frac{H_i}{\Delta H}\right)+1,\ \Delta H_i = \frac{H_i}{N_{H_i}-1}$

  $L_i = L_0 + \sum_{k=1}^{i} \Delta H a^k,\ N_{L_i} = \text{ceil}\left(\frac{L_i}{\Delta H}\right)+1,\ \Delta L_i = \frac{L_i}{N_{L_i}-1}$

  for $j = 0,\dots,N_{L_i}-1$

    $p = p+1,\ x_p = x_0 + j\Delta L_i,\ y_p = y_0 + \frac{H_0}{2}$

    $m_p = \rho_0 \Delta L_i \Delta H_i$

  end for

  for $j = 1,\dots,N_{H_i}-1$

    $p = p+1,\ x_p = x_0 + L_i,\ y_p = y_0 + \frac{H_0}{2} - j\Delta H_i$

    $m_p = \rho_0 \Delta L_i \Delta H_i$

  endfor

  for $j = 1,\dots,N_{L_i}-1$

    $p = p+1,\ x_p = x_0 + L_i - j\Delta L_i,\ y_p = y_0 - \frac{H_0}{2}$

    $m_p = \rho_0 \Delta L_i \Delta H_i$

  end for

endfor

References

[1] Sulsky D, Chen Z, Schreyer HL. A particle method for history-dependent materials. Comput Meth Appl Mech Eng 1994;118(1–2):179–96.

[2] Sulsky D, Zhou S-J, Schreyer HL. Application of a particle-in-cell method to solid mechanics. Comput Phys Commun 1995;87(1–2):236–52.

[3] Sulsky D, Schreyer HL. Axisymmetric form of the material point method with applications to upsetting and Taylor impact problems. Comput Meth Appl Mech Eng 1996;139(1–4):409–29.

[4] Brackbill J, Ruppel H. FLIP: a method for adaptively zoned, particle-in-cell calculations of fluid flows in two dimensions. J Comput Phys 1986;65(2):314–43.

[5] Ionescu I, Guilkey J, Berzins M, Kirby RM, Weiss J. Computational simulation of penetrating trauma in biological soft tissues using the material point method. Stud Health Technol Inform 2005;111:213–8.

[6] Zhou S, Stormont J, Chen Z. Simulation of geomembrane response to settlement in landfills by using the material point method. Int J Numer Anal Meth Geomech 1999;23(15):1977–94.

[7] Wikeckowski Z, Youn S-K, Yeon J-H. A particle-in-cell solution to the silo discharging problem. Int J Numer Meth Eng 1999;45(9):1203–25.

[8] Bardenhagen S, Brackbill J, Sulsky D. The material-point method for granular materials. Comput Meth Appl Mech Eng 2000;187(3–4):529–41.

[9] Tran HD, Sulsky DL, Schreyer HL. An anisotropic elastic-decohesive constitutive relation for sea ice. Int J Numer Anal Meth Geomech 2015;39(9):988–1013.

[10] Guilkey J, Harman T, Banerjee B. An Eulerian–Lagrangian approach for simulating explosions of energetic devices. Comput Struct 2007;85(11–14):660–74.

[11] Zhang F, Zhang X, Sze KY, Lian Y, Liu Y. Incompressible material point method for free surface flow. J Comput Phys 2017;330:92–110.

[12] Stomakhin A, Schroeder C, Chai L, Teran J, Selle A. A material point method for snow simulation. ACM Trans Graph (TOG) 2013;32(4):102.

[13] Ram D, Gast T, Jiang C, Schroeder C, Stomakhin A, Teran J, et al. A material point method for viscoelastic fluids, foams and sponges. In: Proceedings of the 14th ACM SIGGRAPH/Eurographics symposium on computer animation. ACM; 2015. p. 157–63.

[14] Stomakhin A, Schroeder C, Jiang C, Chai L, Teran J, Selle A. Augmented MPM for phase-change and varied materials. ACM Trans Graph (TOG) 2014;33(4):138.

[15] York AR, Sulsky D, Schreyer HL. Fluid-membrane interaction based on the material point method. Int J Numer Meth Eng 2000;48(6):901–24.

[16] Gilmanov A, Acharya S. A hybrid immersed boundary and material point method for simulating 3D fluid-structure interaction problems. Int J Numer Meth Fluids 2008;56(12):2151–77.

[17] Hamad F, Wikeckowski Z, Moormann C. Interaction of fluid-solid-geomembrane by the material point method. Comput Geotech 2017;81:112–24.

[18] Guo Y, Nairn J. Three-dimensional dynamic fracture analysis using the material point method. Comput Model Eng Sci 2006;16(3):141.

[19] Guilkey JE, Weiss JA. Implicit time integration for the material point method: quantitative and algorithmic comparisons with the finite element method. Int J Numer Meth Eng 2003;57(9):1323–38.

[20] Wang B, Vardon PJ, Hicks MA, Chen Z. Development of an implicit material point method for geotechnical applications. Comput Geotech 2016;71:159–67.

[21] Charlton T, Coombs W, Augarde C. iGIMP: an implicit generalised interpolation material point method for large deformations. Comput Struct 2017;190:108–25.

[22] Cummins S, Brackbill J. An implicit particle-in-cell method for granular materials. J Comput Phys 2002;180(2):506–48.

[23] Sulsky D, Kaul A. Implicit dynamics in the material-point method. Comput Meth Appl Mech Eng 2004;193(12–14):1137–70.

[24] Love E, Sulsky D. An unconditionally stable, energy-momentum consistent implementation of the material-point method. Comput Meth Appl Mech Eng 2006;195(33–36):3903–25.

[25] Love E, Sulsky D. An energy-consistent material-point method for dynamic finite deformation plasticity. Int J Numer Meth Eng 2006;65(10):1608–38.

[26] L. Beuth, T. Benz, P.A. Vermeer, Z. Wikeckowski, Large deformation analysis using a quasi-static material point method, J Theor Appl Mech.

[27] Hogan RJ. Fast reverse-mode automatic differentiation using expression templates in C++. ACM Trans Math Software (TOMS) 2014;40(4):26.

[28] Lian Y, Zhang X, Liu Y. Coupling of finite element method with material point method by local multi-mesh contact method. Comput Meth Appl Mech Eng 2011;200(47–48):3482–94.

[29] Chen Z, Qiu X, Zhang X, Lian Y. Improved coupling of finite element method with material point method based on a particle-to-surface contact algorithm. Comput Meth Appl Mech Eng 2015;293:1–19.

[30] Lian Y, Zhang X, Liu Y. Coupling between finite element method and material point method for problems with extreme deformation. Theor Appl Mech Lett 2 (2).

[31] Lian Y, Zhang X, Liu Y. An adaptive finite element material point method and its application in extreme deformation problems. Comput Meth Appl Mech Eng 2012;241:275–85.

[32] Aulisa E, Bná S, Bornia G. FEMuS Web page; 2017. <https://github.com/eaulisa/MyFEMuS>.

[33] Ciarlet PG. Finite element method for elliptic problems. Philadelphia, PA, USA: Society for Industrial and Applied Mathematics; 2002.

[34] Brenner S, Scott R. The mathematical theory of finite element methods, vol. 15. Springer Science & Business Media; 2007.

[35] Zhang X, Chen Z, Liu Y. The material point method: a continuum-based particle method for extreme loading cases. Academic Press; 2016.

[36] Ogden RW. Non-linear elastic deformations. Courier Corporation; 1997.

[37] Capodaglio G, Aulisa E. A particle tracking algorithm for parallel finite element applications. Comput Fluids 2017;159:338–55.

[38] Calandrini S, Aulisa E. Fluid-structure interaction simulations of venous valves: a monolithic ale method for large structural displacements. Int J Numer Meth Biomed Eng 2018. https://doi.org/10.1002/cnm.3156. e3156.

[39] Aulisa E, Bna S, Bornia G. A monolithic ALE Newton–Krylov solver with Multigrid-Richardson-Schwarz preconditioning for incompressible Fluid-Structure Interaction. Comput Fluids 2018;174:213–28.

[40] Calandrini S, Capodaglio G, Aulisa E. Magnetic drug targeting simulations in blood flows with fluid-structure interaction. Int J Numer Meth Biomed Eng 2018;34:e2954.

[41] Aulisa E, Bornia G, Calandrini S. Fluid-structure interaction modeling of artery aneurysms with steady-state configurations. In: VII international conference on computational methods for coupled problems in science and engineering, COUPLED PROBLEMS; 2017. p. 616–27.

[42] Aulisa E, Bornia G, Calandrini S. Fluid-structure simulations and benchmarking of artery aneurysms under pulsatile blood flow. In: 6th ECCOMAS conference - COMPDYN 2017; 2017. p. 955–74.